The prevalence and properties of cold gas inflows and outflows around galaxies in the local Universe

G. W. Roberts-Borsani ⓘ⋆ and A. Saintonge ⓘ
Department of Physics and Astronomy, University College London, Gower Street, London WC1E 6BT, UK

ABSTRACT

We perform a stacking analysis of the neutral Na D $\lambda\lambda$5889, 5895 Å ISM doublet using the SDSS DR7 spectroscopic data set to probe the prevalence and characteristics of cold ($T \lesssim 10^4$ K) galactic-scale gas flows in local ($0.025 \leq z \leq 0.1$) inactive and AGN-host galaxies across the SFR–M_* plane. We find low-velocity outflows to be prevalent in regions of high SFRs and stellar masses ($10 \lesssim \log M_*/M_\odot \lesssim 11.5$), however we do not find any detections in the low-mass ($\log M_*/M_\odot \lesssim 10$) regime. We also find tentative detections of inflowing gas in high-mass galaxies across the star-forming population. We derive mass outflow rates in the range of 0.14–1.74 $M_\odot$ yr^{-1} and upper limits on inflow rates $<1\,M_\odot$ yr^{-1}, allowing us to place constraints on the mass-loading factor ($\eta = \dot{M}_{\rm out}$/SFR) for use in simulations of the local Universe. We discuss the fate of the outflows by comparing the force provided by the starburst to the critical force needed to push the outflow outward, and find the vast majority of the outflows unlikely to escape the host system. Finally, as outflow detection rates and central velocities do not vary strongly with the presence of a (weak) active supermassive black hole, we determine that star formation appears to be the primary driver of outflows at $z \sim 0$.

Key words: ISM: jets and outflows – galaxies: evolution – galaxies: ISM – galaxies: starburst.

1 INTRODUCTION

The Lambda-Cold Dark Matter (ΛCDM) model has been extremely successful in reproducing observations of the large-scale structure of the Universe (e.g. Planck Collaboration I 2016). However, the assumption that the mean growth of DM haloes dictates the cosmological accretion rate of cool gas on to galaxies causes the framework to fail by overpredicting the star formation (SF) activity in low-mass haloes at early times, and in high-mass haloes at later times (Bell et al. 2003; Li & White 2009). The introduction of feedback mechanisms, such as outflows, goes a long way towards reconciling these important discrepancies (Somerville et al. 2008; Bouché et al. 2010) by expelling gas or preventing accretion, and is now regularly invoked in hydrodynamical simulations (e.g. Oppenheimer et al. 2010; van de Voort et al. 2011). The need to accommodate the cycling of gas in and out of galaxies (known as the 'baryon cycle') also brought out new observational frameworks – known as 'bathtub' or 'equilibrium' models (Bouché et al. 2010; Davé, Finlator & Oppenheimer 2012; Lilly et al. 2013) – which place emphasis on the accreted cold gas, the efficiency of star formation, and the role of metal-enriched outflows ejected into the circumgalactic (CGM) and intergalactic medium. These models have now taken centre stage in galaxy evolution (Saintonge et al. 2013) and it is the

interplay between inflows and outflows that dictates the position of a galaxy relative to the 'main sequence' (Noeske et al. 2007) on the SFR–M_* plane, highlighting a necessity for a thorough theoretical and observational understanding of these processes.

Outflows can arise due to large amounts of energy and momentum given off by stellar winds, supernovae, or an active galactic nucleus (AGN). They have been observed and found to be ubiquitous at all epochs (see review by Veilleux, Cecil & Bland-Hawthorn 2005), although most observations have typically focused on a variety of more extreme objects such as mergers, (U)LIRGs, and QSO hosts (e.g. Rupke, Veilleux & Sanders 2005a,b; Cicone et al. 2014; Rupke, Gültekin & Veilleux 2017). Much less is known on the more normal objects at each epoch. Over the past decade, several pioneering studies have helped to observationally constrain the prevalence of low-z ($z \lesssim 1$) outflows in samples of less extreme star-forming galaxies (e.g. Weiner et al. 2009; Chen et al. 2010; Coil et al. 2011; Martin et al. 2012; Rubin et al. 2014). In one of the first major systematic searches, Weiner et al. (2009) used a sample of 1406 DEEP2 galaxy spectra at $z \sim 1.4$ to search for cool, low-ionization outflowing gas and found detections in more than half of their sample. They found evidence that their detection rate had a weak positive dependence on stellar mass and SFR. Martin et al. (2012) followed up on this with an investigation of 200 deep Keck/LRIS spectra of highly star-forming galaxies with $\log M_*/M_\odot > 9.4$ at $0.4 < z < 1.4$. They also found a high detection rate of $\sim$50 per cent, however unlike Weiner et al.

⋆ E-mail: guidowroberts@gmail.com

(2009), they did not find any dependence of outflow properties with stellar mass or SFR. Despite the success of the aforementioned studies in demonstrating the ubiquity of outflows at $z \sim 1$, the selected samples were of a starburst nature and a higher redshift than the present day Universe. Rubin et al. (2014) improved on this with their sample of 105 galaxies derived from the GOODS fields and Extended Groth Strip, at a median redshift $z \sim 0.5$. These objects spanned a larger range of stellar mass (log $M_*/M_\odot \gtrsim 9.6$) and SFRs (SFR $\gtrsim 2$ $M_\odot$ yr^{-1}) than the previous studies. The detection rate for their sample remained high ($\sim$66 per cent), despite sampling lower SFRs. Arguably the most representative study for normal star-forming galaxies of the local Universe, however, was that of Chen et al. (2010). The authors selected a large sample of massive (log $M_*/M_\odot > 10.4$) star-forming galaxies from the Sloan Digital Sky Survey (SDSS; York et al. 2000) at redshifts $0.05 \leq z \leq 0.18$, and by means of stacking found strong and clear dependences of neutral gas outflow properties with galaxy viewing angle, stellar mass, and star formation surface density (Σ_{SFR}).

Each of these studies has found winds to be prevalent in the low-z Universe and, due to them arising in galaxies with high SFRs, has suggested they are generally a consequence of high levels of star formation or Σ_{SFR} – in fact, a critical Σ_{SFR} threshold of 0.1 $M_\odot$ yr^{-1} kpc^2 is regularly suggested in order to launch a galactic wind (Heckman et al. 2002). However, the detection rates of winds have also been found to vary strongly as a function of galaxy disc inclination: working under the assumption that outflows have a biconical structure that exits perpendicular to the disc, one would expect to have fewer detections in absorption at high inclinations (where one views the disc edge-on) and more at low inclination (viewing the disc face-on). Indeed, this appears to be the case, with the majority of detections in absorption arising from low inclinations (Chen et al. 2010; Martin et al. 2012; Rubin et al. 2014). For starburst galaxies with inclinations less than $i \sim 60°$, Heckman et al. (2000) found an $\sim$70 per cent probability of detecting outflows in absorption.

Deep observations of local galaxies also revealed the presence of a diffuse, secondary layer of extraplanar gas (known as a 'lagging halo') that extends kiloparsecs out of the disc. The extraplanar gas has been observed in the atomic (e.g. Fraternali et al. 2002; Matthews & Wood 2003; Oosterloo, Fraternali & Sancisi 2007; Zschaechner, Rand & Walterbos 2015) and ionized (e.g. Rossa & Dettmar 2003a,b; Heald et al. 2007; Kamphuis 2008) gas phases, in both external galaxies and the Milky Way (Marasco & Fraternali 2011). Accompanying the extraplanar gas are often signatures of accretion (e.g. Fraternali et al. 2002; Fraternali & Binney 2008; Zschaechner et al. 2015), and dynamical modelling of the gas suggests outflows or accretion alone cannot account for the observed kinematics and gas masses (Fraternali & Binney 2006). As such, the emerging picture appears to be a cyclic scenario, where gas gets blown out from the disc by stellar winds and supernovae (this 'blowout' phase has been observed by, e.g. Boomsma et al. 2008, who report holes of H I gas in the disc of NGC 6946 with high rates of star formation) and eventually condenses and mixes into colder gas that gets re-accreted and fuels star formation. This scenario is known as the 'galactic fountain' (Shapiro & Field 1976) and plays a crucial role in regulating the gas contents and SFRs of local galaxies.

Although star formation certainly appears to play an important role in launching winds, the dominant energy source for outflows in the present day Universe is not always obvious. Several recent studies have aimed to address this by comparing the detection rates of outflows in local galaxies displaying signatures of star formation

and AGN. For instance, Sarzi et al. (2016) used a sample of 456 objects for which both optical and radio data were available and found that none of the 23 objects displaying signatures of neutral gas outflows showed radio emission or optical line ratios indicative of an AGN. Concas et al. (2017) conducted a similar study with SDSS-selected galaxies and found outflows traced by the same neutral gas to be present in both star-forming galaxies and AGN hosts. These results appear to suggest that weak, optically selected AGNs do not have a major influence on the detection rates of neutral gas outflows. Studies of more extreme AGN/QSOs and starbursts, however, generally portray a more distinct picture: many such objects exhibit very powerful outflows (e.g. Walter, Weiss & Scoville 2002; Cannon et al. 2005; Feruglio et al. 2010; Combes et al. 2013; Cicone et al. 2014; García-Burillo et al. 2015; Fiore et al. 2017) which appear significantly enhanced by the presence of an AGN. For example, using a sample of 19 strong Seyferts, LINERs, and 'pure' starburst galaxies, Cicone et al. (2014) found strong molecular outflows in all galaxy types, but with significantly boosted outflow velocities and mass-loss rates in the AGN hosts. The latter quantity was also found to increase with the AGN luminosity.

These results inevitably lead to the crucial question of whether outflows ultimately halt the SF processes in galaxies (coined 'negative feedback') or not. This can happen via the removal of gas necessary to fuel star formation, prevention of accretion, or a combination of both. Spectroscopic studies have found cases of AGN-driven outflows expelling mass at a rate many times that of the host galaxy's SFR, thereby clearly able to remove significant fractions of gas and eventually quench the host (e.g. Sturm et al. 2011; Cicone et al. 2014). Additionally, some Integral Field Unit (IFU) studies have also shown a spatial coincidence with outflowing material and an absence of SF (e.g. Cresci et al. 2015; Carniani et al. 2016), although it is often unclear whether there is causality in this. Further complicating this picture are instances where star formation has seen itself reignited due to the turbulence created by the presence of an outflow (coined 'positive feedback', e.g. Maiolino et al. 2017; Gallagher et al. 2018). Simulations of the Milky Way even suggest weak outflows form a necessary ingredient to stimulate and *sustain* accretion – and therefore star formation – by transferring gas from a surrounding hot corona to the disc (e.g. Marinacci et al. 2010; Marasco, Fraternali & Binney 2012).

A quantity often used to describe how efficiently outflows can remove mass is the *mass-loading factor*, η, defined as the mass outflow rate divided by the SFR of the host. This value is used in simulations to dictate the strength of outflows (e.g. Oppenheimer et al. 2010; Vogelsberger et al. 2013; Muratov et al. 2015), yet important discrepancies exist with results found in observations, with the latter often finding order-of-magnitude lower values (e.g. Weiner et al. 2009; Martin et al. 2012; Rubin et al. 2014; Chisholm et al. 2017) for normal galaxies. This demonstrates the need to understand whether observations are missing large fractions of ejected mass traced by different gas phases, or simulations are invoking outflows that are larger than those seen in the present day Universe.

Outflows are typically observed via Doppler shifts of ISM gas, characterized by broad components in emission spectra or blueshifted signatures in absorption. The latter method is known as the 'down the barrel' technique, where gas in front of a galaxy is illuminated by the background continuum. Since the gas is moving towards the observer along the line of sight (or 'barrel'), it appears blueshifted with respect to the systemic (galaxy) component. Equally, redshifted absorption is suggestive of gas moving towards the galaxy, in the shape of inflowing gas. Although such signatures may arise from anywhere along the sight line to the galaxy, such that
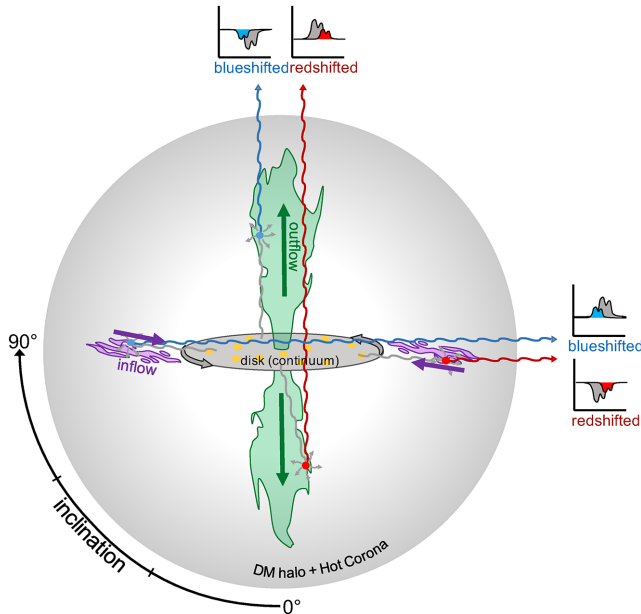
Figure 1. A schematic of the different types of Doppler shifts one can observe in the Na D transition. Foreground gas is dominated by absorption of the background continuum, with profiles either blueshifted (outflows) or redshifted (inflows). Background gas is seen in emission of re-emitted photons. Grey lines represent continuum photons from the galaxy disc, blue lines represent blueshifted signatures, and red lines represent redshifted signatures. Small blue or red circles represent absorption, from which re-emission of the photon occurs. Included in the schematic is the role of the viewing angle in detecting outflowing or potentially inflowing gas.

the technique offers no information as to whether the gas reaches (in the case of an inflow) or fully escapes (in the case of an outflow) the galaxy, red/blueshifted absorption has typically been interpreted as an unambiguous signature of in/outflowing gas relative to the galaxy. A schematic of this method is shown in Fig. 1.

However, the use of different tracers in rest-frame UV or optical wavelengths (e.g. Fe II $\lambda\lambda 2586$, 2600, Mg II $\lambda\lambda 2796$, 2803, Na I D $\lambda\lambda 5890$, 5896, [O III] $\lambda 5007$) and (in many cases) the use of a biased sample (e.g. containing objects selected a priori to have high SFRs, Σ_{SFR}s, or stellar masses) have limited the extent to which general conclusions can be made. An alternative is to use a single tracer and stacking approach over a large and representative sample to create much higher signal-to-noise (S/N) composite spectra, allowing for flow detections over the *general* galaxy population. This is especially useful to probe regions of parameter space that single spectra cannot (e.g. very low M_* or low-SFR galaxies) and derive accurate measurements of flow properties. Recently, similar studies were undertaken using stacked data from the SDSS and other surveys to constrain the properties of and links between neutral and ionized outflows in the general population of galaxies from the low-z Universe (e.g. Chen et al. 2010; Cicone, Maiolino & Marconi 2016; Concas et al. 2017; Sugahara et al. 2017). These studies have allowed for strong constraints on the evolution of outflow properties as a function of key global galaxy parameters (e.g. SFR, M_*, Σ_{SFR}, z, inclination, excitation mechanism). However, still lacking are the crucial constraints on the mass-loading factor, and potential inflowing gas.

In this study, we aim to use the SDSS Data Release 7 (DR7; Abazajian et al. 2009) data set and a stacking technique in order to

sample large ranges of global galaxy properties with which to infer detection rates, properties, and mass flow rates of inflows and outflows. With this, we can place strong constraints on the mass-loading factor in the local Universe. We focus on the resonant Na I absorption doublet at 5889.95 and 5895.92 Å (also referred to as Na D), which traces cool ($T \lesssim 10^4$ K), metal-enriched gas. We present our observational data set and selection criteria in Section 2, stacking and fitting procedures in Section 3, and present our results in Section 4, including details on covering fractions, equivalent widths, mass inflow/outflow rates, central velocities, and the mass-loading factor. Section 5 discusses the implications of our detections and results by offering a comparison to recent simulation results, the role of SF versus AGN feedback, a dissection of the sources of inflow, and a brief discussion on the fate of the outflows. Finally, we summarize our main conclusions in Section 6. Throughout this paper, we adopt a ΛCDM cosmology with $H_0 = 70\,\mathrm{km\,s^{-1}\,Mpc^{-1}}$, $\Omega_m = 0.3$, and $\Omega_\Lambda = 0.7$, and assume a Chabrier IMF.

2 SAMPLE DEFINITION AND MEASUREMENTS

We make use of the full SDSS DR7 catalogues. After requiring all objects to satisfy an SDSSth 'type' of 'GALAXY', we select all objects with a redshift of $0.025 \leq z \leq 0.1$. This redshift range allows for a robust derivation of the galaxy morphology while the SDSS 3 arcsec diameter spectroscopic fibre samples the central $\sim 1.6 - 6.7$ kpc of the galaxy. To separate the AGN hosts from the inactive galaxies, we require a line S/N ratio >3 in all BPT diagnostic lines (namely H α, H β, [O III] $\lambda 5007$, and [N II] $\lambda 6584$) and the satisfaction of a Kauffmann et al. (2003) BPT prescription. If the line S/N ratio of one of the BPT lines is <3, or the galaxy does not satisfy the BPT prescription, it is classified as inactive. This selection yields a parent sample of 240 567 inactive galaxies and 67 753 AGN hosts. We refer to this sample as the main sample. The samples' distributions in redshift, stellar mass, SFR, and Σ_{SFR} are shown in Fig. 2.

For starburst galaxies with inclinations less than $i \sim 60°$, Heckman et al. (2000) found that a high probability (~ 70 per cent) existed of detecting outflows in absorption. This motivates an additional cut to separate galaxies based on their inclination. We therefore define a subsample from our main sample, called DISK, which includes all galaxies with a measurable inclination. In Section 4.2 we show that $i \sim 50°$ is a more suitable inclination cut. We therefore further divide the DISK sample into two subsamples, HIGH-i and LOW-i, with inclinations $>60°$ and $<60°$, respectively. For this, we require an r-band fracDeV parameter of < 0.8 to ensure we select disc galaxies, from which an inclination angle can be calculated from the r-band axial ratio, b/a, as

$$i = \cos^{-1}\left[\left(\frac{(b/a)^2 - q^2}{1 - q^2}\right) - \frac{1}{2}\right], \tag{1}$$

where $q = 0.13$ (Giovanelli et al. 1994) is the assumed intrinsic axial ratio. Finally, we define a BULGE sample with a fracDeV parameter equal to 1 to select objects completely dominated by a bulge. We do not include objects with fracDeV parameters between 0.8 and 1, since these might have some disc structure from which we cannot accurately determine an inclination and therefore do not complement the DISK or BULGE samples. The size of each subsample is listed in Table 1.
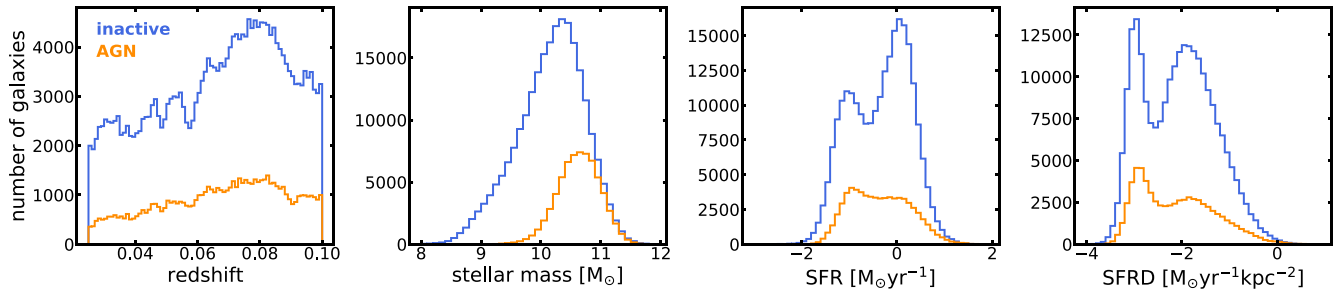
Figure 2. The distributions of redshift, stellar mass, SFR, and Σ_{SFR} of our main samples. The blue histograms represent our inactive galaxies sample and the orange histograms represent our AGN sample.

Table 1. The number of galaxies in each subsample defined for this study.

Sample	Inactive	AGN
main	240 567	67 753
DISK	165 571	32 728
LOW-i	75 739	13 282
HIGH-i	86 558	19 446
BULGE	43 724	19 558

The global galaxy properties associated with our analysis come from the widely used MPA-JHU catalogue,[1] in which the SFRs are derived using the 4000 Å break, following the method of Brinchmann et al. (2004). We derive Σ_{SFR}s ($\Sigma_{SFR} = $ SFR·cos(i)$/\pi r^2$), where r is the physical radius of the galaxy probed by the fibre, in kpc.cna

3 ANALYSIS

3.1 Binning and stacking optical spectra

In order to achieve high S/N, we opt for a spectral stacking analysis over planes of global galaxy properties (e.g. SFR–M_* or i–Σ_{SFR}). Bins are constructed via an adaptive approach, where the edges are defined such that the resulting bin is larger than the mean uncertainty of the relevant property, and the stacked spectrum has a continuum S/N $\geq$ 100. For bins of stellar mass and SFR we require bins larger than 0.2 and 0.5 dex, respectively. The spectra in each bin are first sorted by parameter of interest before being corrected for galactic extinction using the Schlegel dust maps and an O'Donnell et al. (1994) Milky Way extinction curve.

To create the stack, each galaxy spectrum is converted to air wavelengths and shifted to the rest frame, before being interpolated over a common wavelength array. The spectrum is then normalized to the median flux between 5440 and 5550 Å, where it is uncontaminated by emission or absorption lines – this normalization ensures no preferential weighting is given to the lowest redshift galaxies in our sample. The normalized spectrum is then weighted by a mask array (with values of 0 for bad pixels identified in the SDSS spectrum array, and 1 for everything else) and added to the stack. The final stack is then simply the mean over N galaxies with a normalized spectrum, over each wavelength element. The flux uncertainties associated with the composite spectrum are derived by adding in quadrature the mean flux uncertainties calculated from

the SDSS error arrays and the sampling error, which we estimate via a bootstrapping method with replacement.

3.2 Fitting the stellar continuum

The Sodium doublet is a predominantly photospheric transition and is particularly strong in the spectra of cool stars, with peak strengths for stars of types K3-M0 (Jacoby, Hunter & Christian 1984). The prevalence of bulge K-giants in nuclear regions of galaxies means they are likely to make an important contribution to the spectra of this selected sample, since the SDSS fibre probes the central regions of the galaxies at our selected redshifts. Throughout this study, however, we assume the Na D doublet is a feature with additional contributions from the interstellar medium (ISM) and that any signature of in/outflows will be found in this component. As such, the careful removal of any stellar contribution is imperative. To do this, we model the stellar continuum with the Penalized Pixel-Fitting (pPXF; Cappellari 2017) code to fit a non-negative linear combination of Simple Stellar Population (SSP) templates, which make use of the MILES (Sánchez-Blázquez et al. 2006) empirical stellar library, with BaSTI isochrones and [α/Fe]-enhanced models where available. A Battisti, Calzetti & Chary (2016) extinction law is assumed. We carefully mask the Ca II (K and H) and Na D transitions, since these are all in our spectral fitting range, and we assume they are the result of a stellar + ISM contribution, which the models cannot account for. We also mask the red half of the He I emission line at 5875.67 Å, which is close enough to the Na D line that it could affect the residual profile. Furthermore, we allow for non-Gaussian line-of-sight velocity distributions (LOSVDs), since there is a very small possibility this could influence our results if unaccounted for. This is most likely a very minor effect (if present), since our stacking method should blend out such cases and pPXF by definition penalizes non-Gaussian LOSVDs. Additionally, the pPXF software also fits the optical nebular emission lines present in the spectrum. To remove the stellar contribution, the stacked spectrum is divided by the continuum fit. An example stacked spectrum and its best-fitting continuum model are shown in Fig. 3.

To ensure a level of robustness in our continuum fits, we look at the Mg I$\lambda\lambda$ 5167, 5173, 5184 (Mg b) triplet. Since Mg b has a similar ionizing potential as Na D and is produced in similar nuclear processes of hot stars, several studies of Na D outflows in ULIRGs (e.g. Martin 2005; Rupke et al. 2005a,b) estimated the stellar contribution of Na D from Mg b. We instead look at the equivalent width (EW) of the Mg b residuals left over from our continuum fitting: assuming the stellar continuum is well modelled, the residual should be very small and can be used as a proxy for goodness of fit. We find that the distribution of residual EWs is
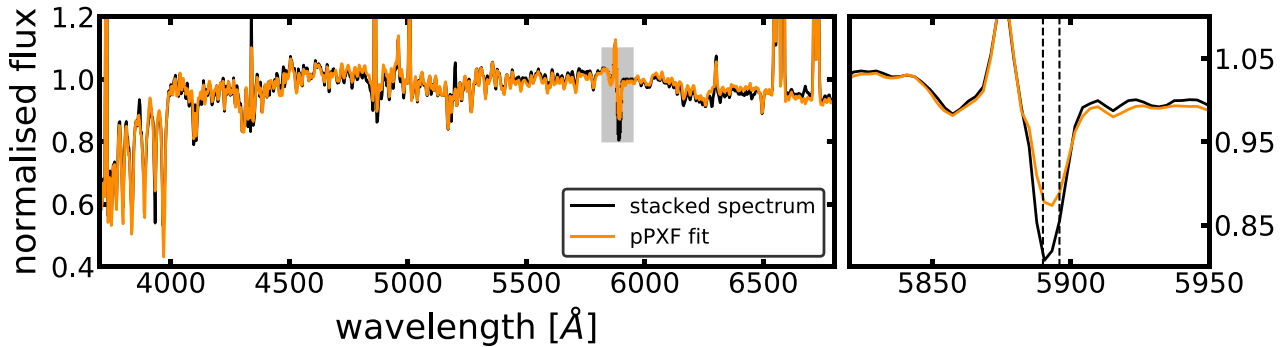
Figure 3. An example stacked spectrum (black) from the inactive main sample, with its best-fitting pPXF continuum (orange). The full spectrum is shown on the left, while the plot on the right is a zoomed-in portion of the grey-shaded region, highlighting the fit to the He I line and the Na D absorption. The dashed lines represent the central blueshifted and redshifted wavelengths of the Na D doublet at 5889 and 5895 Å, respectively.

roughly bimodal, with one mode containing the majority of (small) residuals and the other mode a smaller population of larger residuals, and can be well described by two Gaussian functions. We interpret the larger EWs as a result of poor continuum fitting and define a range of acceptable residuals with a lower limit $\mathrm{EW_{Mg}}b,\text{low} = 0$ Å and an upper limit $\mathrm{EW_{Mg}}b,\text{upp} = 0.112$ Å given by the 1σ width of the main Gaussian containing the small residuals.

3.3 Interpretation of Na D Doppler shifts

Prior to modelling the Na D residual, it is important to consider which types of Doppler shifts we consider to be signatures of outflows and inflows. In the 'Introduction' section, we described how blueshifted or redshifted absorption can be interpreted as foreground gas moving along the line of sight, and therefore as unambiguous signatures of outflows and inflows. Being a resonance transition, Na D also re-emits all absorbed photons isotropically and as such, blueshifted or redshifted resonant *emission* becomes an important consideration. Due to the isotropic nature of the re-emission, on average one cannot have more emission than absorption from forefront gas (the observer sees each absorption signature from the continuum but many re-emitted photons may follow a different sightline), and it is therefore reasonable to assume that absorption dominates the signatures of foreground gas. Following this logic, for a clump of gas on the backside of the galaxy, absorption signatures of the continuum are not visible but photons that are absorbed and then re-emitted by the clump can fall back along the line of sight towards the observer. If the gas is moving away from the observer, the re-emitted photons are redshifted and therefore signatures of outflowing gas, while if they are moving towards the observer then they are blueshifted and signatures of inflowing gas. Several studies (e.g. Chen et al. 2010; Rupke & Veilleux 2015) have demonstrated a correlation between the visibility of redshifted emission and the dust content of the galaxy, suggesting the redshifted emission comes from a backside receding outflow seen through a dust-poor, face-on disc. In some cases redshifted emission is also accompanied by blueshifted absorption (Phillips 1993) in the form of a P-Cygni profile. Additionally, Prochaska, Kasen & Rubin (2011) showed via radiative transfer models of cold gas winds that redshifted emission was in fact a prominent and important feature to consider in outflow studies. Our interpretation of Doppler shifted Na D is consistent with this picture.

To summarize, the sources of inflows and outflows from Doppler shifts (based on geometry) are: blueshifted absorption (outflow),

redshifted absorption (inflow), blueshifted emission (inflow), and redshifted emission (outflow). All of these are highlighted in Fig. 1. However, we note that the line (amplitude) S/N ratios of absorption and emission are significantly different; absorption signatures generally have S/N ratios larger than 10, while emission signatures have ratios less than 10. This is important because it means emission signatures are more sensitive to noise and errors in continuum fitting, as well as residuals from fits to the He I line immediately blueward of Na D. For these reasons, we consider only blueshifted absorption, redshifted absorption, and redshifted emission as signatures of flows, since blueshifted emission is highly sensitive to a larger number of residuals and noise, and therefore much less reliable.

3.4 Bayesian inference and Na D profile fitting

Prior to modelling the residual Na D profile, we fit a first-order polynomial to the flux immediately blueward and redward of the profile and divide the residual by this, to account for any systematic continuum-fitting errors that could give rise to artificial residuals. After this, we are free to fit the ISM residual of Na D with an analytical expression. Because multiple components may contribute to the Na D signal, many degeneracies exist in the profile fitting. For this reason, we employ a Bayesian inference approach using PyMultinest (Buchner et al. 2014), a Python wrapper for the popular nested sampling code, MULTINEST (Feroz, Hobson & Bridges 2009). We make the assumption that our posteriors follow a Gaussian distribution and that our data points are uncorrelated. For our Na D modelling, we use the analytical function described by Rupke et al. (2005a). The model follows the form

$$I(\lambda) = 1 - C_f + C_f \times e^{-\tau_B(\lambda) - \tau_R(\lambda)}, \tag{2}$$

where C_f is the velocity-independent covering factor, and $\tau_B(\lambda)$ and $\tau_R(\lambda)$ are the optical depths of the Na I λ 5891 and Na I λ 5897 lines, respectively. The optical depth of the line, $\tau(\lambda)$, can be expressed as

$$\tau(\lambda) = \tau_0 \times e^{-(\lambda - \lambda_0 + \Delta\lambda_{\text{offset}})^2 / ((\lambda_0 + \Delta\lambda_{\text{offset}}) b_D / c)^2}, \tag{3}$$

where τ_0 and λ_0 are the central optical depth and central wavelength of each line component, respectively, b_D is the Doppler line width, and c is the speed of light. The wavelength offset is converted from a velocity offset, given $\Delta\lambda_{\text{offset}} = \Delta v \lambda_0 / c$. For Na D $\tau_{0,B}/\tau_{0,R} = 2$ (Morton 1991), meaning the Na I λ 5891 line has twice the depth of the Na I λ 5897 line. The optical depth parameter can be derived

Table 2. The priors applied to our model when used for detection and characterization purposes. Note that for emission profiles the covering factor prior changes to $-1 \leq C_f \leq 0$. The free parameters are as follows: $|C_f|$, absolute covering fraction; b_D, Doppler linewidth in km s^{-1}; log N(Na I), column density in cm^{-1}; $|\Delta v_{offset}|$, absolute velocity offset in km s^{-1}.

Parameter	Priors (detection)	Priors (characterization)	
		Systemic	**Flow**
$|C_f|$	0–1	0–1	0–1
b_D (km s^{-1})	20–300	50–450	50–450
log N(Na I) (cm^{-1})	9–15.3	9–15.3	9–15.3
$|\Delta v_{offset}|$ (km s^{-1})	0–200	–	0–500

from the column density of Sodium, which is described as

$$N(\text{Na I}) = \frac{\tau_0 \, b}{1.497 \times 10^{-15} \lambda_0 \, f}, \quad [\text{cm}^{-2}], \tag{4}$$

where λ_0 and f are the rest frame wavelength (vacuum) and oscillator strength, respectively. Throughout this study we assume $\lambda_0 = 5897.55$ Å and $f = 0.318$ (Morton 1991). To determine if an outflow is present, we first fit the Na D line with the model given in equation (4): once assuming $\Delta\lambda_{offset} = 0$ and the second time leaving it as a free parameter. If the model with $\Delta\lambda_{offset} \neq 0$ is preferred, then a flow is present. To determine this, we use a Bayesian Information Criterion (BIC), which makes use of the likelihood for each model but penalizes for additional free parameters. The BIC is defined as

$$\text{BIC} = -2\mathcal{L} + k \cdot \log(N), \tag{5}$$

where $\mathcal{L}$ is the log-likelihood, k is the number of free parameters, and N is the number of data points that get fit. In addition, a minimum velocity offset Δv is required to confirm a flow detection. We discuss the minimum required BIC$_{fixed}$/BIC$_{offset}$ ratio (K) and Δv in Section 3.5. If a flow is detected, we characterize the total profile of the line with a two-component model. In the case of an outflow detection, the profile is also fitted with a three-component model consisting of a systemic component (in absorption), a blueshifted absorption component offset by a minimum of -20 km s^{-1} and a redshifted emission component with $20 < \Delta v_{offset} < 200$ km s^{-1}, in order to be consistent with the findings of Prochaska et al. (2011). All three profiles are allowed a maximum linewidth of 200 km s^{-1}. These priors are chosen so as to restrict the redshifted emission to near-systemic velocities (e.g. Prochaska et al. 2011) and prevent unrealistically large absorption and emission profiles that overfit the data and try to cancel each other out (e.g. Veilleux et al. 2013). A BIC ratio determines the preferred model out of the two, and the final fit is selected accordingly.

The allowed ranges for the parameters in equation (4) are separated in two categories, 'detection' and 'characterization', with the former being slightly more restrictive in linewidth and velocity offset compared to the latter. These are presented in Table 2. The 'detection' ranges apply to single-component fits and the 'characterization' ranges to multiple-component fits. The reasons for this are as follows: (a) we want to limit the amount of degenerate and unrealistic fits that are allowed in the determination of flow detections, e.g. a flow detection could be determined by unrealistically large linewidths and/or velocity offsets that attempt to fit noise or baseline residuals and (b) once a robust detection is found we wish to sample a large parameter range to ensure both the systemic and flow components are well described.

The above procedure works well for profiles of Na D excess in absorption and emission. In Section 4.4 we show that we also find excess in the form of P-Cygni profiles, which are an unambiguous detection of outflows. We are unable to accurately model a systemic galaxy component for such profiles, so we fit the profile with single blueshifted and redshifted double-Gaussian components (e.g. Veilleux et al. 2013). This limitation means we gain no physical information about the state of the gas apart from the velocity shift, which itself can be underestimated as the central wavelength of the Doppler shift will be restricted by the influence of its blueshifted/redshifted counterpart. We therefore assume such outflow velocities to be lower limits and exclude them from our analyses that require information on the physical state of the gas.

3.5 Model completeness and reliability

It is fundamental that the limitations of our fitting models and procedures be understood, and their completeness and reliability quantified. For completeness, we generate synthetic spectra consisting of systemic and offset components. The velocities of the offset components range from -100 to 100 km s^{-1} in 5 km s^{-1} intervals. Each profile is convolved to the FWHM resolution of SDSS with a Gaussian function, before adding random Gaussian noise. This is repeated for three different S/N ratios of 6, 10, and 50 at each velocity offset. The spectrum is then fitted according to our detection technique described in Section 3.4 and the measured blue/redshifted velocity recorded. To ensure the result is not dependent on the random noise added to the spectrum, we repeat this sequence 50 times for each S/N ratio, each with a different random Gaussian noise. The completeness is defined as the fraction of recovered non-zero velocity offsets as a function of input Δv, for each S/N ratio. This is shown in Fig. 4. In the inset plots of Fig. 4 we show the *measured* Δv as a function of input Δv for each completeness plot. Based on these results, we adopt a $|\Delta v|_{input}$ threshold of 40 km s^{-1} for line S/N ratios greater than 10 and 50 km s^{-1} for line S/N ratios less than or equal to 10, which corresponds to >90 and ~85 per cent completeness, respectively. This translates to $|\Delta v|_{output} = 15$ and 20 km s^{-1}, respectively, using the linear $|\Delta v|$ evolution shown in the inset plots of Fig. 4.

Arguably the most important test, however, is the reliability of our detections, since there are a number of factors that could mimic a Doppler shift: the main culprit of this would likely be ISM residuals or artefacts created from bad continuum fitting. For this test, we use our HIGH-i sample (for both inactive galaxies and AGN hosts), which we assume will not display outflows due to unfavourable inclinations. We define bins of SFR–M_* and create 50 stacked bootstrap samples for each bin, in the same fashion as described in Section 3.1. Each stacked spectrum is then fitted with pPXF and the Na D residual put through our detection procedure and all *measured* (output) Δvs are recorded. Since these stacks are meant to represent spectra with no outflow signatures, all detections are considered false positives. The reliability of each bin is defined as the difference between a perfect case of no false positives (100 per cent reliability) and the percentual number of false positives detected out of the 50 stacks, allowed by a set of selection criteria. Our selection criteria should rely on a combination of thresholds given by a K ratio, a minimum measured Δv, and a quantity to guard against residuals left from bad continuum fitting. For this latter consideration, we look at the Mg b absorption residuals, since they are stellar in origin. For the minimum measured velocity we use $|\Delta v|_{output} > 15$ km s^{-1} and $|\Delta v|_{output} > 20$ km s^{-1}, as derived from our completeness tests and $K>1$. The reliability for our samples based on these criteria remains
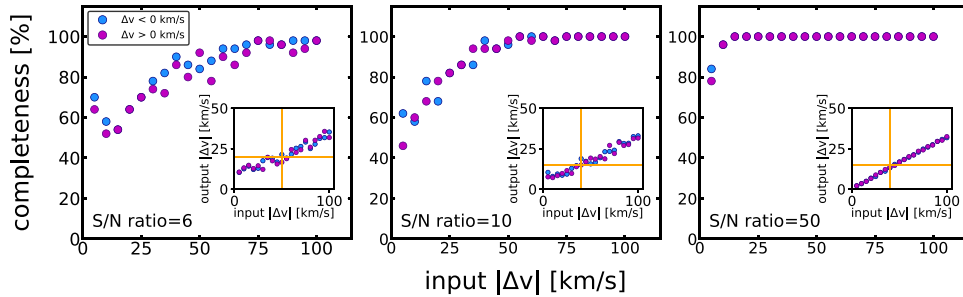
Figure 4. Plots of completeness versus input velocity for our detection procedure. The procedure is calculated for line S/N ratios of 6 (left), 10 (middle), and 50 (right), for both negative offset velocities (blue circles) characteristic of outflows and positive offset velocities (magenta circles) characteristic of inflows. Each inset plot shows the linear evolution of $|\Delta v|_{\mathrm{output}}$ versus $|\Delta v|_{\mathrm{input}}$ in each completeness plot.
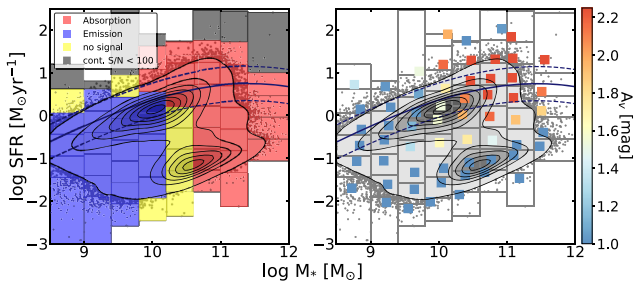

Figure 5. Left: The Na D residual profiles for inactive galaxies from our stacked spectra over the main sample SFR–M_* plane, as a result of the division of the best-fitting continuum given by pPXF. Absorption and emission profiles dominate the high- and low-mass galaxies, respectively, with a separation at $\log M_*/M_\odot \sim 10$–10.5 characterized by low line S/N ratios and P-Cygni profiles. The solid and dashed lines mark the main sequence relation defined by Saintonge et al. (2016), with a +0.35 dex offset in log SFR to account for the different median redshifts of our and their samples. Right: The same plots as the left but with the mean dust A_v values for each stack, highlighting correlation between the dust content and the Na D residual profile.

above 85 per cent over the whole plane. Although our criteria do a good job of guarding against false positive outflow detections, we note that these tests cannot be performed in the same manner for inflowing gas since we have no a priori information on their angle of incidence. However, the selected thresholds should also limit the number of false positive inflow detections, since the main culprit for these would be bad continuum fitting, which we account for.

4 STACKING RESULTS

4.1 Na D profiles across the SFR–M_* plane

The profiles (absorption, emission, P-Cygni, or unknown) of the Na D residual in each stack are identified via visual examination, and reveal a stark bimodality in type occurring between low-mass ($\log M_*/M_\odot < 10$) and high-mass ($\log M_*/M_\odot > 10$) galaxies, with the former showing average profiles in emission and the latter in absorption. A few profiles at $\log M_*/M_\odot \sim 10$–10.5 have near-zero line amplitude or show a P-Cygni profile. This distribution is shown in Fig. 5 and is similar to the distribution of Sodium excess found by Concas et al. (2017). The change in Na D profile type with stellar mass is most likely attributed to the nebular dust attenuation in each stack. It is well known that Na D has a low ionizing potential (5.14 eV) and therefore requires dust shielding

and high gas filling factors in the ISM for its survival. At high mass, galaxies have sufficient amounts of dust to allow Na D to survive and therefore absorb incident photons. Inclination can also play an important role, since highly inclined galaxies are viewed along the plane of the disc, with an increased quantity of intervening dust. The exception to these rules are red sequence galaxies below the main seqfuence, which have low dust contents and filling factors yet still show profiles in absorption. We find that in such cases the EW of the Na D residual correlates with the Mg b residual, and is therefore attributed to template mismatch – we do not consider flow detections in these galaxies.

At low masses ($\log M_*/M_\odot \lesssim 10$–10.5) the Na D profile is seen in emission. The reasons for this are not fully understood. As discussed in Chen et al. (2010), this could be due to a template mismatch in the continuum fitting. While we cannot completely rule out this possibility, we greatly reduce such a risk by constructing very high S/N stacked spectra and by checking the quality of our continuum fits through the Mg b residual. Another possibility is that the emission excess is caused by our choice of SSP models and continuum-fitting code. In Appendix A, however, we demonstrate that the strong $\log M_*/M_\odot$ dependence on the ISM profile is reproduced using several different codes and SSP models. Finally, due to the fact it is possible to observe Na D in emission, we must also consider that these profiles are real: a decrease in continuum intensity with stellar mass results in a reduced absorption line profile, since absorbed photons become scarce. However, a non-negligible fraction of the re-emitted photons still make their way to the observer to 'fill in' (Martin et al. 2012) the near-absent absorption. The resulting net profile can therefore be in emission if enough photons are re-emitted along the line of sight. Since absorption occurs along many other sightlines from the galaxy, re-emission from these can also be scattered towards the observer and contribute to the line profile. Such an effect is only seen in cases of scarce absorption at low mass (due to a weaker continuum). This is also observed with other resonant absorption lines (e.g. Martin et al. 2012). Over all SFR–M_* stacks for inactive and AGN galaxies we find absorption profiles in ~50 per cent of all high-continuum S/N bins, emission profiles in ~35 per cent, P-Cygni profiles in ~0.3 per cent, and ~14 per cent of profiles are classified as 'unknown'.

4.2 Flow detection rates and inclination dependence

4.2.1 i–Σ_{SFR} plane

Many studies have found strong dependences of outflow detection rates on Σ_{SFR} (Heckman et al. 2000) and inclination (e.g. Chen et al.
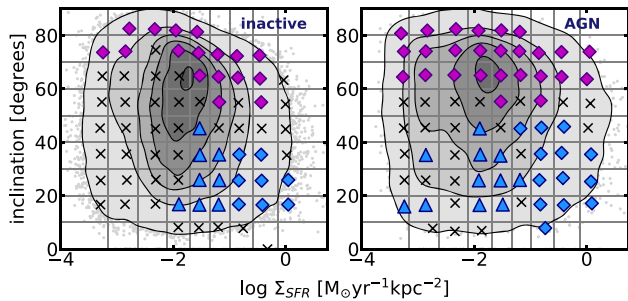
Figure 6. The inclination and Σ_{SFR} dependence of inflows and outflows for our DISK sample. The left- and right-hand panels show the results for the inactive and AGN objects, respectively. The symbol and colour convention follow those of Fig. 7.

2010; Concas et al. 2017). To test the prevalence of inflows and outflows in our sample, we therefore begin by analysing the Na D ISM component in bins of i–Σ_{SFR} for the DISK sample. The results of the stacks are shown in Fig. 6 for inactive galaxies and AGN hosts. We also observe a clear dependence of outflow detections on Σ_{SFR} and inclination: outflows are found most prominently in face-on systems that are characterized by low inclinations ($i < 50°$) and high Σ_{SFR}s. Heckman et al. (2000) found outflows to be ubiquitous above a threshold of $\Sigma_{SFR} > 0.1\,\mathrm{M_\odot\,yr^{-1}\,kpc^{-2}}$ and with low ($i < 60°$) inclinations. Our results decrease the former threshold by an order of magnitude (to $0.01\,\mathrm{M_\odot\,yr^{-1}\,kpc^{-2}}$) and reduce the latter to $i < 50°$ (in agreement with results found by Concas et al. 2017). We measure the detection rate of outflows as the number of bins with detections divided by the total number of bins in a sample or set of thresholds. The detection rate over these thresholds is 74 per cent (inactive and AGN). All detections with $\Sigma_{SFR} > 0.1\,\mathrm{M_\odot\,yr^{-1}\,kpc^{-2}}$ are characterized by profiles in absorption, while those with $0.01 < \Sigma_{SFR} < 0.1\,\mathrm{M_\odot\,yr^{-1}\,kpc^{-2}}$ are found in emission or via P-Cygni profiles, highlighting the necessity to consider all sources of Doppler shifted gas.

We also find a large number of inflow detections in regions of high inclinations ($i > 50°$) and a large range of Σ_{SFR}s, with a detection rate that mildly increases with higher Σ_{SFR}s. Such a clear inclination dependence for inflowing gas has not been seen before, with several studies claiming contrasting results: e.g. Rubin et al. (2012) found that out of a sample of six disc-like galaxies, five displayed inflow at signatures at high inclinations ($i > 55°$), yet Martin et al. (2012) reported that out of four galaxies reporting inflows, only one had a similarly high inclination ($i \sim 61°$) and the remaining three had low inclinations ($i < 55°$; Kornei et al. 2012).

The properties of the i–Σ_{SFR} detections are discussed throughout the rest of Section 4, although due to the slightly uncertain nature of the detections in emission, we focus only on detections in absorption, where the nature of the residual is better understood.

4.2.2 *SFR–M_* plane*

From the above results, we can now repeat our analysis over the SFR–M_* plane for our samples of disc galaxies with inclinations less or greater than $i = 50°$, and bulge-dominated objects. The results for these are shown in Fig. 7. Similarly to our findings over the i–Σ_{SFR} plane, we find a high number of outflow detections in star-forming regions (log SFR$\gtrsim 0\,\mathrm{M_\odot\,yr^{-1}}$) of high-mass (log $M_*/\mathrm{M_\odot} \gtrsim 10$) galaxies with low inclinations. Detections are found in absorption, emission, and in P-Cygni profiles. No outflow detec-

tions are found in low-mass (log $M_*/\mathrm{M_\odot} \lesssim 10$) galaxies or galaxies with high inclinations. This applies to both inactive galaxies and AGN hosts. The detection rates and median galaxy-host properties of our detections are shown in Table 3, while the properties of the gas flows are presented in Tables B1 and B2. For bins with log SFR$> -0.5\,\mathrm{M_\odot\,yr^{-1}}$ – which roughly coincides with the lower limit of the star-forming main sequence at low mass – over our LOW-i and BULGE samples, we find an outflow detection rate of 53.5 per cent.

We find detections of inflows in star-forming galaxies with high inclinations. No inflow detections are found in low-inclination galaxies or bulge-dominated galaxies. If we apply the same SFR lower limit as above to the HIGH-i sample, we find an inflow detection rate of 43.7 per cent for inactive galaxies and AGNs.

4.3 Covering fractions

The covering fraction of the flow, C_f, is a measure of the local clumpiness of the gas along the line of sight. In Tables B1 and B2 we report the covering fractions determined by our analysis for inactive galaxies and AGN hosts, respectively. For each of our samples, the covering fractions span the full range of allowed values and there appears to be no difference between the covering fractions of outflows and inflows. We note, however, that in many cases we also find flows characterized by very low covering fractions, $|C_f| \lesssim 0.25$. Unlike for point sources at high redshift where the gas completely covers the background source, for low-redshift sources where the background source subtends a large angle on the sky, a covering fraction less than unity is not unexpected. However, such low covering fractions are likely not a result of geometry alone. Very low fractions have also been observed by Chen et al. (2010), who stack over similar samples of galaxies. One explanation to describe such low values is that we are observing small amounts of neutral Na D gas with low dust shielding in very dense clouds within the outflow, where ionizing radiation and shocks no longer dominate.

4.4 Equivalent widths

The EW of a line is a measure of its strength and therefore can provide information about the strength of an outflow or inflow. Fig. 8 plots the distributions of EWs measured from fits to our Na D absorption profiles over the i–Σ_{SFR} and SFR–M_* planes. The measurements are also presented in Tables B1 and B2. Fig. 8(a) plots the distribution of the *total* line EW. We report a narrow range of outflow EWs ($0 < \mathrm{EW_{NaD}} < 1.2$) for the combined inactive and AGN samples, with a median 0.24 Å and a standard deviation 0.26 Å. These values are similar to those found by Chen et al. (2010) but have a median that is an order of magnitude smaller than that found by Rupke et al. (2005b), who report a median of 3.3 Å and a maximum of value 9.1 Å for Na D in (U)LIRGs. The higher values found by Rupke et al. (2005b) are most likely attributed to the increased column densities found in their samples, while Chen et al. (2010) study galaxies more closely matched to this sample. We note that our AGN samples have a slightly higher median value of 0.29 Å compared to 0.25 Å for inactive galaxies, and a higher maximum value of 1.2 Å (AGN) compared to 0.93 Å (inactive). A Kolmogorov–Smirnov (K–S) test between the two distributions, however, reveals a low coefficient of 0.16, suggesting the two distributions are still very similar.

The difference in reported values between Rupke et al. (2005b) and the distributions in Fig. 8(a) clearly illustrates the difference in outflow strength between normal galaxies and more extreme
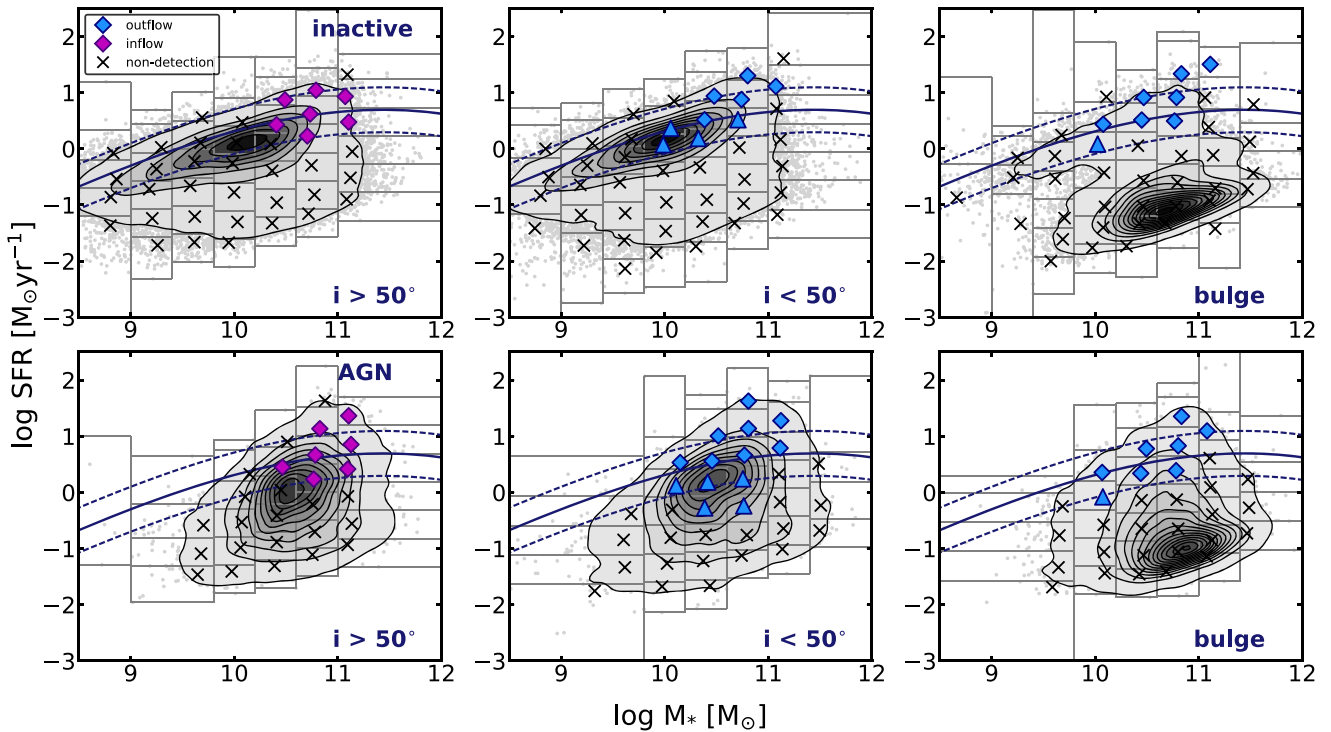
Figure 7. The detections of inflows and outflows across the SFR–M_* plane for disc galaxies (left and middle columns) separated by inclination, and bulge galaxies for which inclinations cannot be accurately established (right column). The top row shows our sample of inactive galaxies while the bottom row is for AGN hosts.

Table 3. The detection rate of inflows and outflows in the SFR–M_* plane across all bins with a continuum S/N>100, and median properties of their galaxy hosts.

Sample	Inactive		AGN	
	Inflows	Outflows	Inflows	Outflows
HIGH-i	18 %	0 %	26 %	0 %
LOW-i	0 %	20 %	0 %	39 %
BULGE	0 %	19 %	0 %	26 %
Median properties of host Galaxy				
SFR ($M_\odot$ yr^{-1})	4.15	3.29	4.64	3.63
Σ_{SFR} ($M_\odot$ yr^{-1} kpc^{-2})	0.09	0.21	0.12	0.11
M_* (log $M_\odot$)	10.73	10.47	10.82	10.75
nebular A_v (mag)	2.94	2.20	3.22	2.35
D_n4000	1.42	1.30	1.45	1.35
Concentration index	2.45	2.53	2.54	2.43

Figure 8. (a): The distribution of total EWs for inactive galaxies and AGNs. The grey bars represent the full distribution, while the blue bars represent outflow detections and inflows are marked by the magenta bars. Black bars are non-detections. (b): A comparison of the EWs measured blueward and redward of the 5889 and 5895 Å Na I lines, where outflows (blue) and inflows (magenta) are expected to be seen, respectively. The dotted black line is a straight line fit to the systemic components (black x's) while the dashed blue and magenta lines are best-fitting linear functions to outflow and inflow detections, respectively. (c) histogram distributions of the EW$_{blue}$/EW$_{red}$ ratio for inflows, outflows, and non-detections. The orange vertical lines represent our suggested cuts to isolate each distribution.

objects. By preselecting systems with large Na D residuals, it is likely that a large number of weaker outflow signatures would be overlooked. In Fig. 8(b) we show an alternative measurement of EW, where we plot the EW of the flux blueward of the Na I 5889 Å line versus the EW of the flux redward of the Na I 5895 Å line. A clear separation of outflow detections, inflow detections, and non-detections becomes evident, which is not apparent from measurements of the *total* EW of the Na D doublet. A histogram of the EW$_{blue}$/EW$_{red}$ ratio is shown in Fig. 8(c) and three distinct distributions appear. By applying a cut of EW$_{blue}$/EW$_{red}$ > 1.35 for outflows and a cut of EW$_{blue}$/EW$_{red}$ < 0.75 for inflows, one selects 100 per cent of outflow detections and 86 per cent of inflow detections, with only ∼10 per cent contamination from
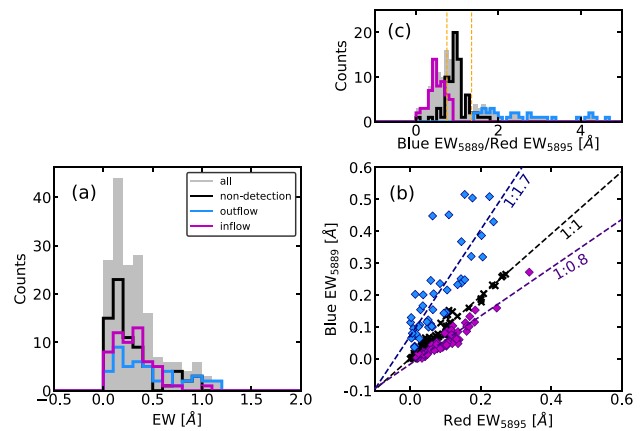
the non-detections (subject to uncertainties in the EW measurements). Using 'edge-EWs' instead of the total EW of Na D provides a more complete and unbiased way to select potential outflow candidates.

4.5 Flow velocities

The central velocity of a flow is a measure of the velocity at which the bulk of the material is travelling. In Fig. 9 we plot the central velocity measurements of inflow and outflow detections in absorption as a function of global galaxy properties, and compare them to results in the literature that study samples of outflows in galaxies at $z < 1$. The stacks shown in these plots are created from a sample of high-mass (log $M_*/M_\odot > 10$) and high-Σ_{SFR} ($\Sigma_{SFR}s > 0.1\,M_\odot\,yr^{-1}\,kpc^{-2}$) DISK galaxies, since in Sections 4.2 and 4.2.2 we have shown these thresholds to be important in finding outflows. The left-hand panel of Fig. 9 shows stacks binned by i-log SFR, while the points in the right-hand panel are binned by i-log M_*.

We report absolute outflow velocities in the range 69–370 km s^{-1} with a median of 160 km s^{-1}, consistent with results for samples of normal star-forming galaxies (e.g. Chen et al. 2010; Martin et al. 2012; Rubin et al. 2012, 2014). Our reported values are not characteristic of particularly high outflow velocities compared to some cases of extreme starburst or AGN hosts, which are able to launch ~1000–2000 km s^{-1} outflows with different gas phases (e.g. Tremonti, Moustakas & Diamond-Stanic 2007; Chung et al. 2011; Cicone et al. 2014; Carniani et al. 2015). We find no significant difference between outflow velocities from the inactive sample compared to the AGN hosts: we report medians of 155 km s^{-1} (inactive) and 167 km s^{-1} (AGN), with maximum central velocities of 234 km s^{-1} (inactive) and 370 km s^{-1} (AGN). This suggests that while the presence of an optically selected AGN might slightly enhance an outflow's velocity, it does not do so by a significant amount.

In the left-hand panel, we see there appears to be little to no correlation of outflow velocity with total SFR (unlike in, e.g. Heckman et al. 2015) within our sample, although the scatter appears to increase with SFR. We also note that a correlation may not appear present due to the small range of SFRs probed by our stacks, which also appears to be the case in Chen et al. (2010) for a near-identical sample and SFR range. In the right-hand panel we also find little to no correlation between outflow velocity and increasing stellar mass. Inflow velocities are also consistent with the results from the studies mentioned above, spanning a range 139–193 km s^{-1} with a median central velocity of 151 km s^{-1}. Only an ~6 km s^{-1} difference exists between the median inactive and AGN inflow velocities. Furthermore, we find no correlations of velocity with SFR or stellar mass.

It is important to note that none of these velocities have been corrected for inclination, and as such they may be (and are likely to be) underestimated (we observe a difference of ~20–30 km s^{-1} between the inclination-corrected and uncorrected median outflow velocities in Fig. 9). Since the velocity offset is used in several calculations (e.g. the mass outflow rates in Section 4.6), this underestimation is propagated throughout the analysis and therefore such outflow quantities serve as lower limits. We present the inclination-corrected velocities in Tables B1 and B2, however do not use these in our plots for the sole purpose of facilitating a comparison with other results in the literature, which also use uncorrected velocities.

4.6 Mass outflow rates and mass-loading factor

Two of the most important quantities one can derive in studies of galactic-scale flows are the mass outflow rate ($\dot{M}_{out}$) and mass-loading factor (η), which describes the rate of mass ejected from the galaxy per unit of SFR. These measurements help quantify the rate at which galaxies are expelling mass and the extent to which they

are able to quench the star formation. Before deriving these rates, however, there are several important assumptions to consider. For a spherically symmetric, mass conserving wind that travels at velocity v, the average mass flow rate across a radius r can be expressed as the following:

$$\dot{M}_{out} = \Omega\,\mu\,m_H\,N(H)\,v\,r\,, \tag{6}$$

where Ω is the solid angle subtended by the wind at its origin (i.e. the global covering factor of the wind), m_H is the mean atomic weight (with a $\mu = 1.4$ correction for relative He abundance), $N(H)$ is the column density of Hydrogen along the line of sight, v is the central velocity of the wind, and r is the distance from the galaxy.

Here we make the same assumptions made by Rupke et al. (2005b) and refer the reader to their paper for details. In short, we assume a solid angle less than 4π, a radius of 5 kpc, and that the column density of Hydrogen can be expressed as

$$N(H) = \frac{N(Na\,I)}{\chi(Na\,I)\,d(Na\,I)\,Z(Na\,I)}, \tag{7}$$

where $N(Na\,I)$ is the Sodium column density, $\chi(Na\,I) = N(Na\,I)/N(Na)$ is the assumed ionization fraction, $d(Na\,I)$ is the depletion on to dust, and $Z(Na\,I)$ is the Na abundance. We assume a 90 per cent ionization fraction [$\chi(Na\,I) = 0.1$], a Galactic value (Savage & Sembach 1996) for the depletion on to dust [log $d(Na\,I) = -0.95$], and solar metallicity ($Z(Na\,I) = \log[N(Na)/N(H)]_\odot = -5.69$). We report a wide distribution of total outflow column densities for our i–Σ_{SFR} and SFR–M_* stacks of $17.85 < \log N(H)/cm^{-2} < 21.98$, with a median of 19.77 cm^{-2}. We observe little difference between the medians of the inactive objects (19.46 cm^{-2}) and AGN hosts (19.89 cm^{-2}). These values are similar (albeit slightly lower) to those observed for (U)LIRGs at low-z (Rupke et al. 2005b; Cazzoli et al. 2016). The distribution of column densities for the inflows is somewhat narrower and shifted towards lower values, with a range $18.94 < \log N(H)/cm^{-2} < 20.28$ and median 19.60 cm^{-2}.

From the above assumptions, equation (6) can be expressed as

$$\dot{M}_{out} = 11.5 \sum \left(\frac{C_\Omega}{0.4}\,C_f\right)\left(\frac{r}{10\,kpc}\right)$$
$$\times \left(\frac{N(H)}{10^{21}\,cm^{-2}}\right)\left(\frac{|\Delta v|}{200\,km\,s^{-1}}\right) M_\odot\,yr^{-1}. \tag{8}$$

Fig. 10 shows the derived mass outflow rates versus SFR for the i-SFR stacks, and we compare these to the (U)LIRGs of Rupke et al. (2005b) and Cazzoli et al. (2016), as well as the H II galaxies of Fluetsch et al. (2018), who all use the same tracer and similar assumptions. All uncertainties associated with our calculated values incorporate those from the fit free parameters. We note that the main drivers of the mass outflow uncertainties are the covering factor and the assumed radius of the wind. We report mass outflows rates of $-0.83 \lesssim \log \dot{M}_{out}/M_\odot\,yr^{-1} \lesssim 0.24$ for an SFR range of $-0.16 \lesssim \log SFR/M_\odot\,yr^{-1} \lesssim 1.23$. These rates are similar to those found by Rubin et al. (2012) for galaxies of similar stellar mass but slightly higher redshift ($z \sim 0.5$). Our detections extend to lower SFRs. We find that mass-loss rates are generally ~10 per cent of the SFR and that a positive (linear) correlation between the two quantities exists with a near-constant mass-loading factor $\eta \approx 0.1$. The relation has a measured Pearson coefficient of $r_p = 0.85$ using our data only and a slight decreased coefficient $r_p = 0.77$ when also using the results from Rupke et al. (2005b), Cazzoli et al. (2016), and Fluetsch et al. (2018). A first-order polynomial fit to our data returns

$$\log \dot{M}_{out} = (1.08 \pm 0.17) \cdot \log SFR - (1.05 \pm 0.14). \tag{9}$$
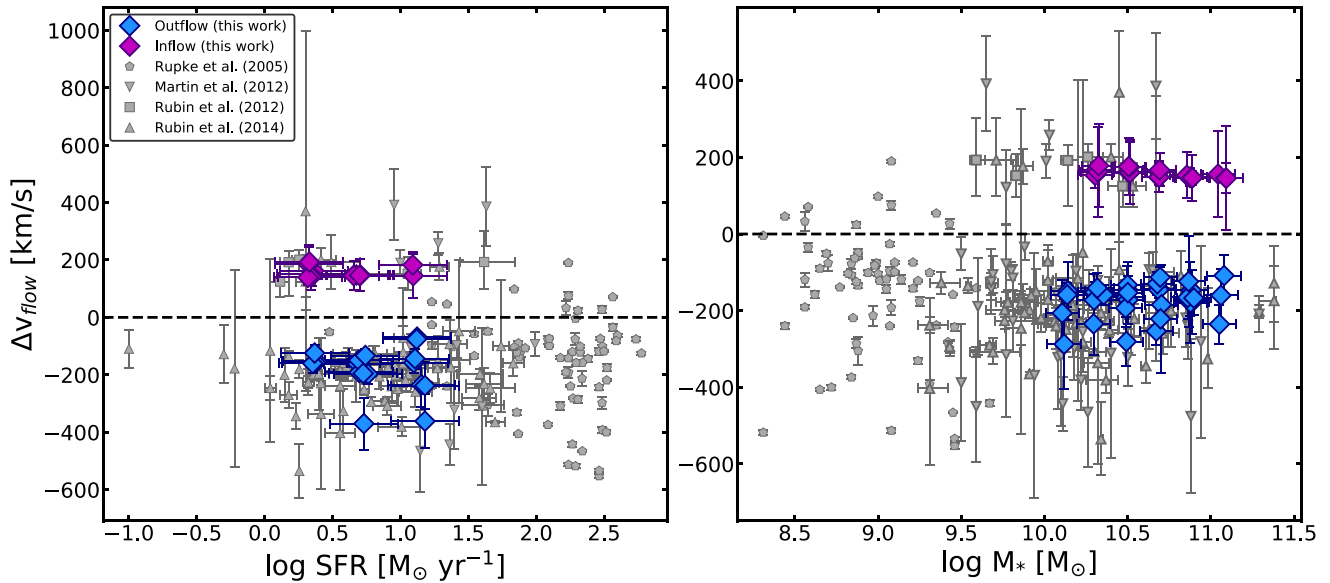
Figure 9. Left: The central inflow and outflow velocities (uncorrected for inclination) as a function of SFR. Right: The same as the left-hand panel but as a function of stellar mass. Results from Rupke et al. (2005a,b), Martin et al. (2012), Rubin et al. (2012), and Rubin et al. (2014) are overplotted for a comparison, where available. The symbol and colour convention follow those of Fig. 7.
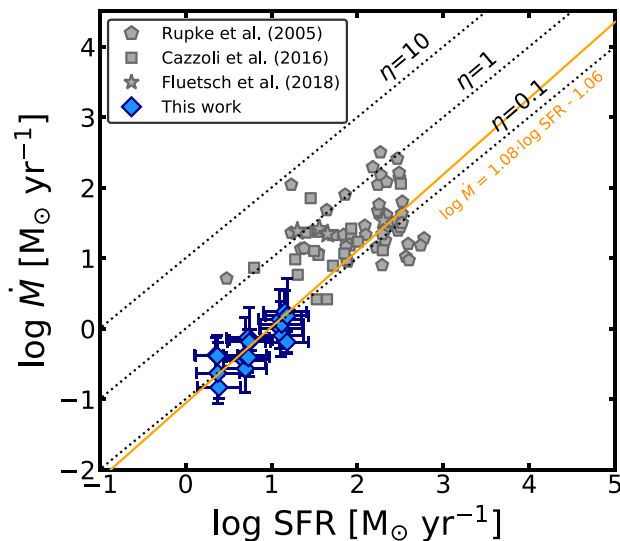
Figure 10. The mass outflow rates for the LOW-*i* samples of inactive and AGN galaxies. A first-order polynomial fit to our data is shown in orange. Overplotted are the results from Rupke et al. (2005b) (grey pentagons) and Fluetsch et al. (2018) (blue stars), where available.

The near constancy of η is perhaps surprising, however such a value is consistent with other low factors observed in studies of similar objects (e.g. Veilleux et al. 2005; Martin et al. 2012; Rubin et al. 2014), suggestive of low-z starbursts and Milky Way-type galaxies being unable to drive strong winds (defined by high mass-loading factors). We also note a mean difference of $0.11\,\mathrm{M}_{\cdot}\,\mathrm{yr}^{-1}$ between inclination-corrected outflow rates and the uncorrected rates presented above.

4.7 Comparison to other gas phases

In the previous section we derived mass outflow rates using the Na D tracer of neutral gas. However, this is only one gas phase and does not account for the molecular and ionized gas phases, which likely contribute non-negligible amounts of ejected gas. A direct and comprehensive comparison is challenging due to the lack of uniform data sets, however some studies have made notable attempts. Recently, Fluetsch et al. (2018) looked at molecular outflows with ALMA CO data and cross-matched their sample with optical data (where available). They found that for star-forming galaxies the ratio of molecular mass outflow rates ($\dot{M}_{H_2}$) to ionized ($\dot{M}_{ion}$) mass outflow rates was close to unity, while AGN hosts displayed much stronger molecular mass outflow rates (correlating with AGN luminosity). Of particular interest to this study is the comparison of $\dot{M}_{H_2}$ to the atomic mass outflow rates ($\dot{M}_{H_I}$): for their sample of AGN hosts, they find $\dot{M}_{H_2}$ is generally ∼1 order of magnitude higher than $\dot{M}_{H_I}$ using Na D. However, for their star-forming sample large scatter dominates and prevents a clear conclusion. To work around this, an alternative tracer (C +) is used and the ratio $\dot{M}_{H_2}/\dot{M}_{H_I}$ is found to be roughly equal for AGNs. They tentatively conclude that for starburst-driven galaxies, the ionized, atomic, and molecular phases contribute in roughly equal quantities to the total mass outflow rate. As such, it is likely our mass outflow rates are only lower limits and a multiwavelength estimation of such rates would lead to more complete and slightly higher values, given the added mass from the other gas phases.

4.8 Upper limits on mass inflow rates

In Figs 6 and 7 we find detections of inflowing gas among disc galaxies. The infalling gas could come from cosmological filaments, from galactic fountains, minor mergers, or from gas cooling from the CGM. Due to the uncertain source of the inflows, the assumptions made for equation (8) may not hold. In particular, assumptions

about the metal content, ionization fraction, and depletion on to dust become highly uncertain when converting to a column density of Hydrogen. None the less, we can assume these as upper limits to convert to mass inflow rates, since it is likely metallicity and abundances would decrease outside of the galaxy disc. With this in mind, we report upper limit inflow rates of 0.08–0.38 $M_\odot$ yr^{-1}. No significant trend is found with the SFRs or stellar mass of the galaxies.

In Fig. 7 we see that inflows have a strong inclination dependence, and are only seen at high ($i > 50°$) inclinations. This suggests that we are seeing the gas accreting along the plane of the disc. Ho et al. (2017) used Mg II absorption and quasar sightlines to probe the CGM of a sample of 15 highly inclined, local star-forming galaxies with known rotation curves. They showed that much of the Doppler shifted Mg II gas was consistent with the rotational motion of the host galaxies and the implication for this was radial infall of gas into the disc plane. It is possible that our results suggest a similar scenario, where inflowing gas (from a variety of sources) falls radially before becoming dominated by the circular motions of the galaxy disc.

5 DISCUSSION

5.1 The prevalence of outflows and inflows

Several studies have claimed a ubiquity of outflows over the star-forming main sequence (e.g. Weiner et al. 2009; Rubin et al. 2014). Our results are partially consistent with this picture in that outflows appear prevalent in star-forming systems with SFR>1 $M_\odot$ yr^{-1} or $\Sigma_{SFR} \geq 0.01\,M_\odot$ yr^{-1} kpc^{-2} and stellar masses log $M_*/M_\odot > 10$. We do not, however, find outflows in low-mass galaxies. Reasons for this could be due to lower Σ_{SFR}s or limitations of Na D as a tracer (e.g. in the absence of dust). We therefore cannot claim ubiquity over the whole of the main sequence. Additionally, we find that outflows are also found in bulge-dominated objects with sufficiently high SFRs, and therefore are not dependent on morphology. We find this to be true for both AGN and inactive galaxies.

5.2 Comparison to simulations

In this section, we compare the flothw properties derived in this study to results from simulations, namely those of Muratov et al. (2015) and Anglés-Alcázar et al. (2017) using the Feedback in Realistic Environments (FIRE) simulations at $z< 0.5$, as well as those from Oppenheimer et al. (2010).

(i) *The prevalence of inflows and outflows in star-forming galaxies.*
The prevalence of outflows in our samples of star-forming galaxies appears only partially consistent with results from simulations. Both Muratov et al. (2015) and Oppenheimer et al. (2010) find that high-mass galaxies have stable discs and a more continuous, quiescent mode of star formation at $z < 1$ that can no longer drive very *strong* outflows into the halo. Dwarf galaxies instead maintain a bursty state of star formation that allows them to produce outflows (Muratov et al. 2015). Our results both agree and contrast with these simulations in that we find low-velocity outflows to be common among star-forming galaxies with high stellar mass but no detections in low-mass (log $M_*/M_\odot < 10$) galaxies, whose Σ_{SFR}s are significantly lower. If outflows are indeed present at low-mass, it is possible that we are unable to detect them due to (a) the outflows being too weak for our code to detect, or (b) a resolution issue

where the velocities are blended by the SDSS spectral resolution, or (c) the unreliability of Na D as a tracer in low-A_v environments

The above simulations also predict non-negligible amounts of accreting gas on to star-forming galaxies. Our study agrees with this, as we find inflow detections in star-forming, high-mass disc galaxies. The source of the inflowing gas is impossible to ascertain from our data, however it is likely a combination of material coming from pristine cold gas, gas from nearby companions, minor mergers, and/or recycled gas ('galactic fountains').

(ii) *Outflow central velocities and mass-loading factors.*
By using the M_*–M_h relation described in Behroozi, Wechsler & Conroy (2013) and equation (1) in Mo & White (2002), we are able to compare the central velocities of our outflow detections to those reported in simulations, as a function of halo circular velocity, v_c. We find our central velocities are within the broad range of median velocities ($20 \lesssim \Delta v \lesssim 4000$ km s^{-1}) reported by Muratov et al. (2015) and lie right on the power-law relation calibrated for their medium-z ($0.5 < z < 2.0$) and high-z ($2.0 < z < 4.0$) samples. However, our velocities appear more than an order of magnitude larger than the upper limits of their L^* progenitors at $z <0.5$, which have velocities less than 100 km s^{-1}.

We also compare our mass-loading factors to those found in simulations and find them to be in agreement with the upper limits for the low-z L^* progenitors of Muratov et al. (2015). Muratov et al. (2015) make an approximate comparison between their mass-loading factors and those derived in the Illustris project (Vogelsberger et al. 2013), and find the Illustris results to be systematically higher than theirs ($\eta \approx 7$ for a Milky Way-mass galaxy at $z = 0$, compared to $\eta \ll 1$). Although we caution a direct comparison due to the differences by which the mass-loading factors are measured in each study, such high mass-loading factors are in contrast with our results and suggest some prescriptions may be adopting abnormally strong outflows than what are typically seen in the local Universe.

5.3 Star formation versus AGN

Several recent studies have discussed the implications of AGNs on the baryon cycle and their influence in the launching of outflows. In these studies, the Na D tracer was used to detect outflows in samples of AGN and star-forming galaxies and determine which energy source was the primary driver of the outflows. For example, Sarzi et al. (2016) used SDSS spectra of 456 local star-forming galaxies from the mJIVE-20 survey to determine whether these hosted both an optical outflow and showed radio emission as part of the Very Large Array's (VLA) FIRST survey. Not a single object showed an outflow detection together with radio emission and therefore the authors concluded outflows were regulated by star formation, not AGN feedback. Nedelchev, Sarzi & Kaviraj (2017) also compared the effects of AGN feedback in a sample of ~9900 SDSS Seyfert 2 galaxies and a control sample of ~44 000 inactive galaxies. Only 0.5 per cent of their Seyfert 2 sample displayed potential outflows compared to 0.8 per cent for the control sample, suggesting AGN activity did not enhance outflow activity. Fig. 7 from our study extends these results to the regime of normal star-forming galaxies and modest AGNs. As reported in Sections 4.5 and 4.6, there is a mild increase in outflow velocity and mass outflow rates with the presence of an AGN, although the differences between the median inactive and AGN values are only ~12 km s^{-1} and ~0.34 $M_\odot$ yr^{-1}. Such small values suggest these AGNs do not *significantly* enhance outflow activity or strength. We can therefore conclude that the presence of an optically selected AGN does not significantly enhance outflows in *normal* galaxies of the local Universe, and that
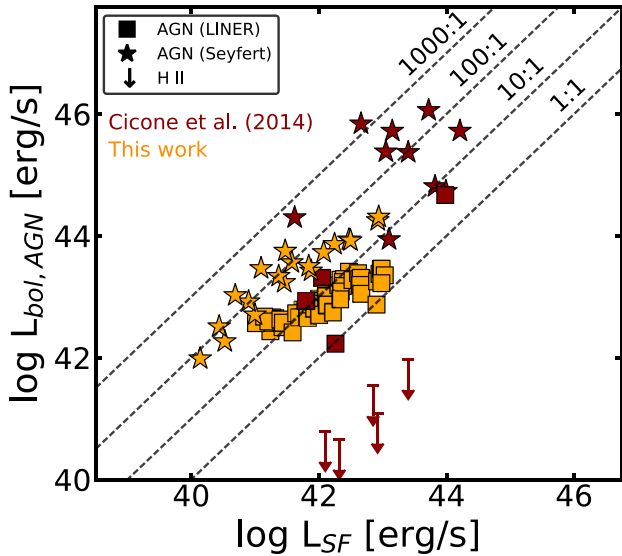
Figure 11. A comparison of the energy output from the AGN (L_{AGN}) and from star formation (i.e. supernovae, L_{SF}) for our AGN stacked sample (orange) and objects from Cicone et al. (2014) (red). Additionally, we extract and stack the Seyfert objects in our AGN sample and plot the data points for a comparison. The dashed lines denote $L_{bol, AGN}/L_{SF} = 1000$, 100, 10, and 1.

Figure 12. *Left*: The outflow velocity as a function of the galaxy's circular velocity, compared to the results of Heckman et al. (2015). Blue stars are the inactive galaxies and the red stars are the AGN of the i-log M_* sample. *Right*: A comparison of the momentum flux (or force) provided by the galaxy starburst versus the critical momentum flux necessary for the net force acting on a cloud to be outward. The dashed diagonal lines denote $\dot{p}_*/\dot{p}_{crit} = 10$, 1, and 0.1 as well as three outflow regimes: 'no outflow', 'weak outflow', and 'strong outflow'.

such winds are unlikely to be able to quench a galaxy via 'ejective' feedback, where gas is removed from the galaxy via the outflow.

This may appear somewhat at odds with recent observations of strong AGN feedback in both the local and high-z Universe (e.g. Feruglio et al. 2010; Alatalo et al. 2011; Maiolino et al. 2012; Cicone et al. 2014), however there are several plausible reasons for this. The first is that we may not be observing the same types of AGNs: our BPT cut and binning procedure ensure we are selecting and mixing weak AGNs that could be drowning out much of the signal produced by rarer and much stronger AGNs (e.g. Seyferts). This is highlighted in Fig. 11, where we compare the energy output from the AGN versus the energy output of supernovae.

The AGN luminosity is calculated using equation (3) of Netzer (2009), which makes use of the [O III] and [O I] luminosities, while the energy output of star formation (i.e. supernovae) is derived using the relation presented by Veilleux et al. (2005):

$$L_{SF} = 7 \times 10^{41} \text{SFR}(M_\odot \text{ yr}^{-1}) \text{ [erg s}^{-1}]. \tag{10}$$

For a comparison, we plot the quantities (where available) for the sample of Cicone et al. (2014) and also stacked spectra of the Seyferts within our AGN sample (selected with an additional BPT cut of log [O III]/H β > 0.5).

As evident from the plot, the AGN feedback found by the aforementioned studies is observed in extreme objects that host very strong AGNs, not typical of the samples of galaxies that we probe. We find a median luminosity (uncorrected for dust) log $L_{AGN, bol} = 42.8$ erg s^{-1} over the DISK AGN sample. For a comparison, the median log L_{AGN} of Cicone et al. (2014)'s extended sample is log $L_{AGN} = 44.76$ erg s^{-1} – about two orders of magnitude higher. This highlights the comparative weakness of optically selected AGN in normal galaxies. Additionally, it is important to note that SF can significantly contribute to the [O III] flux and therefore deducing an accurate L_{AGN} value from this method is challenging. These values are, in essence, upper limits of the true AGN energy contribution.

Nevertheless, a comparison of AGNs in normal star-forming objects – not just in extreme objects – remains useful towards constraining the extent to which an active nucleus may impact the prevalence and properties of galactic winds.

A second, less likely, reason is to do with the dynamical time-scales of AGN activity and outflows: it is possible that we are also observing (a) objects with AGNs that are in the process of turning off due to reduced rates of gas accretion and/or (b) outflows that are relics of the strong feedback found in more extreme objects or at high-z. All of these scenarios are consistent with our observations and findings and our study does not rule out strong feedback by more extreme AGNs.

5.4 The fate of outflows

Several useful quantities exist to obtain an approximation of an outflow's energy relative to the gravitational well of the host galaxy. In Fig. 12(a) we plot the outflow velocity versus the circular velocity (v_{circ}) of the host galaxy for stacks over the i-log M_* plane, and add the results of Heckman et al. (2015) for local star-forming galaxies for a comparison. This provides us with an idea of whether an outflow is travelling at speeds close to the escape velocity of the galaxy or not. The circular velocity is derived from the stellar mass of the host galaxy: $v_{circ} = \sqrt{2}S$, where S is the kinematic parameter (Weiner et al. 2006; Kassin et al. 2007) found to have a good fit with stellar mass for low-z star-forming galaxies, log $S = 0.29$ log $M_* - 0.93$ (Heckman et al. 2015; Simons et al. 2015). We see that most of our detections (23/33) lie below the 1:1 line, suggesting the outflow velocity does not exceed the circular velocity of the host. However, we also notice there are some detections (10/33) that have outflow velocities greater than the circular velocity of the galaxy. These all occur in the lower mass systems, suggesting that outflowing gas may become unbound from the galaxy's gravitational potential.

Another useful comparison is of the force provided by the host galaxy's starburst (caused by stellar winds, supernovae, and radiation pressure) to the critical force needed to have a net force acting outward on the outflow. Assuming a momentum-driven outflow consisting of a population of filamentary clouds (e.g. Chevalier & Clegg 1985) dense enough to produce the observed absorption line profile (e.g. the outflow in M82), the momentum flux (or force) provided by the starburst is $\dot{p}_* = 4.8 \times 10^{33}$ SFR and the critical momentum flux acting on a cloud needed for the net force acting on

it to be outward is $\dot{p}_{crit} = 4\pi r_* N(H) m_H v_{circ}^2$ (for more details, see section 4 of Heckman et al. 2015). In Fig. 12(b) we plot these two quantities for the LOW-*i* SFR–M_* stacks and compare them to the results of Heckman et al. (2015). We find that 10/12 detections fall under the 'weak-outflow' regime defined by Heckman et al. (2015), where the starburst provides $\dot{p}_* \sim$1–10 $\dot{p}_{crit}$, and 2/12 detections fall under the 'no-outflow' regime where $\dot{p}_* < \dot{p}_{crit}$ and the starburst cannot match or exceed the force needed to overcome gravity. None of our detections fall in the 'strong-outflow' regime where $\dot{p}_* > 10\dot{p}_{crit}$ and the outflow exceeds the escape velocity of the galaxy.

These basic results provide rough approximations of the force provided to the outflows and suggest the vast majority of our detections are unable to escape the host galaxy's gravitational hold. In fact, such arguments are based on ballistic models that do not account for the presence of a surrounding gaseous corona, while in reality hydrodynamical processes should play a crucial role in slowing down the outflow, making it even more difficult to escape the galaxy system. This is likely to play an even more important role in the most massive systems, since they reside in denser environments (Oppenheimer & Davé 2008). Given the low velocities of our inflow/outflow detections, the inclination dependence, and the relatively low median SFRs of our stacks, it is likely we are viewing aspects of a galactic fountain scenario, where the gas is expelled from the galaxy disc into the surrounding medium, before it mixes and cools with potential pristine gas to fall back down into the disc as an inflow. The low velocities are unlikely to be enough to escape the host system and it is therefore not unreasonable to assume these outflows could be fuelling (in part) the extra-planar gas observed in external galaxies (e.g. Fraternali et al. 2002; Rossa & Dettmar 2003a; Oosterloo et al. 2007) and the Milky Way (Marasco & Fraternali 2011). The simultaneous detections of outflows *and* inflows in virtually the same regions of parameter space – separated only by inclination effects – are most easily explained by the scenario of a galactic fountain (Fraternali & Binney 2006).

6 SUMMARY AND CONCLUSIONS

In this study we conduct a stacking analysis of 240–567 inactive galaxies and 67 753 AGN hosts from the SDSS DR7 survey. We stack spectra over bins of global galaxy properties and place constraints on the detection rates and properties of inflows and outflows in the local Universe. Our main conclusions can be summarized as the following:

(i) Signatures of outflowing gas are detected along the main sequence of star-forming galaxies for a large range of stellar masses ($10 \lesssim \log M_*/M_\odot \lesssim 11.5$). We also find detections of inflows in star-forming, disc galaxies over a similar range of stellar mass ($10 \lesssim \log M_*/M_\odot \lesssim 11$). These results hold for both inactive galaxies and AGN hosts.

(ii) We find a strong inclination dependence for the detection rates of both outflows and inflows in disc galaxies, with outflows prevalent at low inclinations ($i \lesssim 50°$) and inflows at high inclinations ($i \gtrsim 60°$). This is suggestive of outflowing gas perpendicular to the galaxy disc and accretion along the plane of the disc. Galaxy morphology does not appear to play a major role in the detection rates of outflows.

(iii) We report low ($\sim$0.14–1.74 $M_\odot$ yr^{-1}) mass outflow rates and compare these to other results in the literature. These comparisons reveal a strong linear relationship between the mass outflow

rate and the SFR of the host galaxy, and a prescription is provided. The mass-loading factor, given by the ratio of these two quantities, is calculated to be near-constant ($\eta \approx 0.1$) for local, normal star-forming objects.

(iv) We find only minor differences in outflow detection rates and properties of inactive and AGN galaxies, suggesting that the presence of a weak AGN does not significantly enhance either. Neither galaxy type appears able to launch winds strong enough to quench a galaxy.

Galaxy-scale outflows are an integral element of galaxy evolution models. They play a key role in shaping the environments and mass build-up of galaxies across cosmic time. Here we have studied outflows in stacks of large samples of local galaxies over a range of stellar mass and SFRs and found them to be common among star-forming galaxies. However, none of the outflows are powerful enough to quench their hosts via ejective feedback, but may none the less be able to significantly influence the surrounding environments of the galaxies. To verify this, more work is required to link the properties of outflows to the gas content and distribution in the CGM. To obtain a better understanding and a more comprehensive picture of outflows, large dedicated surveys (UV, optical, and submillimetre) and IFU observations of neutral, ionized, and molecular gas in normal star-forming objects are required in order to constrain and link the multiwavelength nature of outflows. Such observations would also allow more concrete constraints on the geometries of outflows, which have until now relied on crude and unconstrained assumptions. Finally, still required are detailed analyses of inflows and their interplay with outflows and the host galaxies. In combination with simulations that track the accretion of pristine, merged, and recycled gas, such observations would greatly complement and enhance our knowledge of the conditions necessary to fuel star formation across cosmic time.

REFERENCES

Abazajian K. N. et al., 2009, ApJS, 182, 543

Alatalo K. et al., 2011, ApJ, 735, 88

Anglés-Alcázar D., Faucher-Giguère C.-A., Kereš D., Hopkins P. F., Quataert E., Murray N., 2017, MNRAS, 470, 4698

Battisti A. J., Calzetti D., Chary R.-R., 2016, ApJ, 818, 13

Behroozi P. S., Wechsler R. H., Conroy C., 2013, ApJ, 770, 57

Bell E. F., McIntosh D. H., Katz N., Weinberg M. D., 2003, ApJS, 149, 289

Boomsma R., Oosterloo T. A., Fraternali F., van der Hulst J. M., Sancisi R., 2008, A&A, 490, 555

Bouché N. et al., 2010, ApJ, 718, 1001

Brinchmann J., Charlot S., White S. D. M., Tremonti C., Kauffmann G., Heckman T., Brinkmann J., 2004, MNRAS, 351, 1151

Bruzual G., Charlot S., 2003, MNRAS, 344, 1000

Buchner J. et al., 2014, A&A, 564, A125

Cannon J. M., Skillman E. D., Sembach K. R., Bomans D. J., 2005, ApJ, 618, 247

Cappellari M., 2017, MNRAS, 466, 798

Carniani S. et al., 2015, A&A, 580, A102

Carniani S. et al., 2016, A&A, 591, A28

Cazzoli S., Arribas S., Maiolino R., Colina L., 2016, A&A, 590, A125

Chen Y.-M., Tremonti C. A., Heckman T. M., Kauffmann G., Weiner B. J., Brinchmann J., Wang J., 2010, AJ, 140, 445

Chevalier R. A., Clegg A. W., 1985, Nature, 317, 44

Chisholm J., Tremonti C. A., Leitherer C., Chen Y., 2017, MNRAS, 469, 4831

Chung A., Yun M. S., Naraynan G., Heyer M., Erickson N. R., 2011, ApJ, 732, L15

Cicone C. et al., 2014, A&A, 562, A21

Cicone C., Maiolino R., Marconi A., 2016, A&A, 588, A41

Coil A. L., Weiner B. J., Holz D. E., Cooper M. C., Yan R., Aird J., 2011, ApJ, 743, 46

Combes F. et al., 2013, A&A, 558, A124

Concas A., Popesso P., Brusa M., Mainieri V., Thomas D., 2017, A&A, preprint (arXiv:1710.08423)

Cresci G. et al., 2015, ApJ, 799, 82

Davé R., Finlator K., Oppenheimer B. D., 2012, MNRAS, 421, 98

Feroz F., Hobson M. P., Bridges M., 2009, MNRAS, 398, 1601

Feruglio C., Maiolino R., Piconcelli E., Menci N., Aussel H., Lamastra A., Fiore F., 2010, A&A, 518, L155

Fiore F. et al., 2017, A&A, 601, A143

Fluetsch A., et al., 2018, preprint (arXiv:1805.05352)

Fraternali F., Binney J. J., 2006, MNRAS, 366, 449

Fraternali F., Binney J. J., 2008, MNRAS, 386, 935

Fraternali F., van Moorsel G., Sancisi R., Oosterloo T., 2002, AJ, 123, 3124

Gallagher R., Maiolino R., Belfiore F., Drory N., Riffel R., Riffel R. A., 2018, MNRAS, preprint (arXiv:1806.03311)

García-Burillo S. et al., 2015, A&A, 580, A35

Giovanelli R., Haynes M. P., Salzer J. J., Wegner G., da Costa L. N., Freudling W., 1994, AJ, 107, 2036

Heald G. H., Rand R. J., Benjamin R. A., Bershady M. A., 2007, ApJ, 663, 933

Heckman T. M., 2002, in John S. M., John S., eds, ASP Conf. Ser. Vol. 254, Extragalactic Gas at Low Redshift. Astron. Soc. Pac., San Francisco, p. 292

Heckman T. M., Lehnert M. D., Strickland D. K., Armus L., 2000, ApJS, 129, 493

Heckman T. M., Alexandroff R. M., Borthakur S., Overzier R., Leitherer C., 2015, ApJ, 809, 147

Ho S. H., Martin C. L., Kacprzak G. G., Churchill C. W., 2017, ApJ, 835, 267

Jacoby G. H., Hunter D. A., Christian C. A., 1984, ApJS, 56, 257

Kamphuis P., 2008, PhD thesis

Kassin S. A. et al., 2007, ApJ, 660, L35

Kauffmann G. et al., 2003, MNRAS, 346, 1055

Kornei K. A., Shapley A. E., Martin C. L., Coil A. L., Lotz J. M., Schiminovich D., Bundy K., Noeske K. G., 2012, ApJ, 758, 135

Li C., White S. D. M., 2009, MNRAS, 398, 2177

Lilly S. J., Carollo C. M., Pipino A., Renzini A., Peng Y., 2013, ApJ, 772, 119

Maiolino R. et al., 2012, MNRAS, 425, L66

Maiolino R. et al., 2017, Nature, 544, 202

Marasco A., Fraternali F., 2011, A&A, 525, A134

Marasco A., Fraternali F., Binney J. J., 2012, MNRAS, 419, 1107

Marinacci F., Binney J., Fraternali F., Nipoti C., Ciotti L., Londrillo P., 2010, MNRAS, 404, 1464

Martin C. L., 2005, ApJ, 621, 227

Martin C. L., Shapley A. E., Coil A. L., Kornei K. A., Bundy K., Weiner B. J., Noeske K. G., Schiminovich D., 2012, ApJ, 760, 127

Matthews L. D., Wood K., 2003, ApJ, 593, 721

Morton D. C., 1991, ApJS, 77, 119

Mo H. J., White S. D. M., 2002, MNRAS, 336, 112

Muratov A. L., Kereš D., Faucher-Giguère C.-A., Hopkins P. F., Quataert E., Murray N., 2015, MNRAS, 454, 2691

Nedelchev B., Sarzi M., Kaviraj S., 2017, MNRAS, preprint (arXiv:1705.07994)

Netzer H., 2009, MNRAS, 399, 1907

Noeske K. G. et al., 2007, ApJ, 660, L43

O'Donnell J. E., 1994, ApJ, 422, 158

Oosterloo T., Fraternali F., Sancisi R., 2007, AJ, 134, 1019

Oppenheimer B. D., Davé R., 2008, MNRAS, 387, 577

Oppenheimer B. D., Davé R., Kereš D., Fardal M., Katz N., Kollmeier J. A., Weinberg D. H., 2010, MNRAS, 406, 2325

Phillips A. C., 1993, AJ, 105, 486

Planck Collaboration I, 2016, A&A, 594, A1

Prochaska J. X., Kasen D., Rubin K., 2011, ApJ, 734, 24

Rossa J., Dettmar R.-J., 2003a, A&A, 406, 493

Rossa J., Dettmar R.-J., 2003b, A&A, 406, 505

Rubin K. H. R., Prochaska J. X., Koo D. C., Phillips A. C., 2012, ApJ, 747, L26

Rubin K. H. R., Prochaska J. X., Koo D. C., Phillips A. C., Martin C. L., Winstrom L. O., 2014, ApJ, 794, 156

Rupke D. S., Veilleux S., Sanders D. B., 2005a, ApJS, 160, 87

Rupke D. S., Veilleux S., Sanders D. B., 2005b, ApJS, 160, 115

Rupke D. S. N., Veilleux S., 2015, ApJ, 801, 126

Rupke D. S. N., Gültekin K., Veilleux S., 2017, ApJ, 850, 40

Saintonge A. et al., 2013, ApJ, 778, 2

Saintonge A. et al., 2016, MNRAS, 462, 1749

Sánchez-Blázquez P. et al., 2006, MNRAS, 371, 703

Sarzi M., Kaviraj S., Nedelchev B., Tiffany J., Shabala S. S., Deller A. T., Middelberg E., 2016, MNRAS, 456, L25

Savage B. D., Sembach K. R., 1996, ARA&A, 34, 279

Shapiro P. R., Field G. B., 1976, ApJ, 205, 762

Simons R. C., Kassin S. A., Weiner B. J., Heckman T. M., Lee J. C., Lotz J. M., Peth M., Tchernyshyov K., 2015, MNRAS, 452, 986

Somerville R. S., Hopkins P. F., Cox T. J., Robertson B. E., Hernquist L., 2008, MNRAS, 391, 481

Sturm E. et al., 2011, ApJ, 733, L16

Sugahara Y., Ouchi M., Lin L., Martin C. L., Ono Y., Harikane Y., Shibuya T., Yan R., 2017, ApJ, 850, 51

Tremonti C. A., Moustakas J., Diamond-Stanic A. M., 2007, ApJ, 663, L77

van de Voort F., Schaye J., Booth C. M., Dalla Vecchia C., 2011, MNRAS, 415, 2782

Veilleux S., Cecil G., Bland-Hawthorn J., 2005, ARA&A, 43, 769

Veilleux S. et al., 2013, ApJ, 776, 27

Vogelsberger M., Genel S., Sijacki D., Torrey P., Springel V., Hernquist L., 2013, MNRAS, 436, 3031

Walter F., Weiss A., Scoville N., 2002, ApJ, 580, L21

Weiner B. J. et al., 2006, ApJ, 653, 1027

Weiner B. J. et al., 2009, ApJ, 692, 187

York D. G. et al., 2000, AJ, 120, 1579

Zschaechner L. K., Rand R. J., Walterbos R., 2015, ApJ, 799, 61

APPENDIX A: COMPARISON OF SSP MODELS

To ensure the distribution of line residuals we discuss in Section 4.1 is not dependent (to within reasonable margins of uncertainty) on the codes or SSP models used in our study, we repeat our continuum fitting on the main sample for inactive galaxies using a custom made PYTHON continuum-fitting code in combination with the codes from

Bruzual & Charlot (2003) and Maraston & Strömbäck (2011). We make use of both the MILES and STELIB libraries for each code and compare these to the results derived in pPXF. The results are presented in Fig. X. The distribution of residual Na D ISM profiles remains constant throughout all four cases, demonstrating that this result is independent of the choice of SSP models or codes.
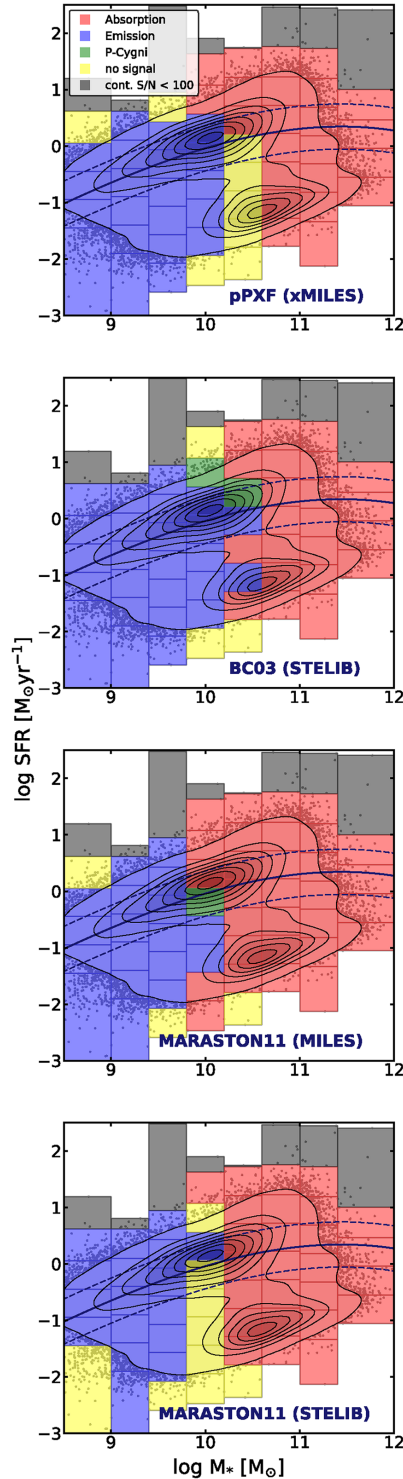

Figure A1. The distribution of Na D ISM profiles across the SFR–M_* plane derived by dividing the stacked spectrum in each bin by the best-fitting continuum obtained using the code and SSP models stated on the bottom right of each plot.

APPENDIX B: NA D FITTING PROPERTIES

Table B1. The properties of the flow parameters measured over the DISK, HIGH-*i*, LOW-*i*, BULGE, *i*-log SFR, and *i*-log M_* samples for inactive galaxies. For profiles with blueshifted absorption and redshifted emission, a *b* postscript indicates the blueshifted component, while the *r* postscript refers to the redshifted component of the profile.

Sample	SFR	log M_*/M$_\odot$	EW	Δv	Δv/cos(*i*)	b_D	C_f	N(Na I)	N(H)	Profile	Type
DISK	0.13	10.59	0.07	147 ± 49	521	118 ± 43	0.75 ± 0.26	11.94	19.61	Absorption	Inflow
–	0.18	10.09	0.06	133 ± 20	484	136 ± 19	0.84 ± 0.26	11.86	19.54	Absorption	Inflow
–	0.21	9.63	0.06	69 ± 132	535	97 ± 104	0.71 ± 0.28	11.90	19.58	Absorption	Inflow
–	0.36	9.89	0.07	67 ± 19	503	111 ± 20	0.87 ± 0.25	11.88	19.56	Absorption	Inflow
–	1.08	9.94	0.01^b	-260 ± 87^b	-271^b	61 ± 42^b	0.26 ± 0.27^b	11.58^b	19.25^b	Absorption	Outflow
–	–	–	-0.24^r	21 ± 5^r	22^r	199 ± 10^r	-0.06 ± 0.01^r	13.84^r	21.52^r	Emission	Outflow
–	0.67	10.06	0.05	77 ± 7	284	117 ± 8	0.83 ± 0.22	11.79	19.47	Absorption	Inflow
–	0.70	10.18	0.04	173 ± 15	1226	71 ± 13	0.50 ± 0.25	11.82	19.50	Absorption	Inflow
–	1.48	10.04	0.02^b	-260 ± 64^b	-271^b	56 ± 35^b	0.48 ± 0.26^b	11.36^b	19.04^b	Absorption	Outflow
–	–	–	-0.20^r	25 ± 10^r	26^r	200 ± 10^r	-0.04 ± 0.00^r	13.98^r	21.66^r	Emission	Outflow
–	1.50	10.00	0.01^b	-235 ± 25^b	-262^b	70 ± 15^b	0.90 ± 0.23^b	11.04^b	18.72^b	Absorption	Outflow
–	–	–	-0.22^r	22 ± 7^r	25^r	200 ± 3^r	-0.05 ± 0.00^r	13.86^r	21.54^r	Emission	Outflow
–	1.43	10.02	0.01^b	-210 ± 20^b	-256^b	77 ± 11^b	0.49 ± 0.23^b	11.30^b	18.97^b	Absorption	Outflow
–	–	–	-0.22^r	21 ± 3^r	26^r	198 ± 1^r	-0.05 ± 0.00^r	13.91^r	21.59^r	Emission	Outflow
–	1.39	10.04	0.01^b	-282 ± 13^b	-401^b	51 ± 6^b	0.40 ± 0.24^b	11.27^b	18.95^b	Absorption	Outflow
–	–	–	-0.12^r	21 ± 2^r	29^r	200 ± 1^r	-0.02 ± 0.00^r	14.45^r	22.13^r	Emission	Outflow
–	1.14	10.12	0.04	82 ± 7	193	104 ± 7	0.89 ± 0.21	11.61	19.29	Absorption	Inflow
–	1.10	10.24	0.04	180 ± 7	631	50 ± 5	0.46 ± 0.23	11.76	19.43	Absorption	Inflow
–	1.09	10.27	0.04	170 ± 125	1128	80 ± 75	0.84 ± 0.26	11.61	19.28	Absorption	Inflow
–	1.79	10.08	-0.05	245 ± 45	256	175 ± 33	-0.63 ± 0.25	11.90	19.57	Emission	Outflow
–	1.95	10.11	-0.06	267 ± 30	297	178 ± 29	-0.94 ± 0.24	11.76	19.44	Emission	Outflow
–	1.84	10.10	-0.04	286 ± 19	351	170 ± 17	-0.84 ± 0.24	11.67	19.35	Emission	Outflow
–	1.76	10.17	0.01	195 ± 7	341	50 ± 3	0.32 ± 0.25	11.62	19.30	Absorption	Inflow
–	1.69	10.25	0.03	184 ± 6	428	50 ± 4	0.88 ± 0.25	11.45	19.13	Absorption	Inflow
–	1.73	10.37	0.05	186 ± 11	631	66 ± 13	0.22 ± 0.25	12.32	20.00	Absorption	Inflow
–	2.60	10.17	0.11	-184 ± 56^b	-193^b	–	–	–	–	P-Cygni	Outflow
–	–	–	-0.06	184 ± 73^r	192^r	–	–	–	–	P-Cygni	Outflow
–	2.71	10.22	0.18	-35 ± 28^b	-39^b	–	–	–	–	P-Cygni	Outflow
–	–	–	-0.13	158 ± 15^r	175^r	–	–	–	–	P-Cygni	Outflow
–	2.81	10.22	0.00^b	-91 ± 60^b	-112^b	163 ± 34^b	0.43 ± 0.17^b	10.18^b	17.86^b	Absorption	Outflow
–	–	–	-0.09^r	180 ± 6^r	220^r	197 ± 2^r	-0.02 ± 0.00^r	13.83^r	21.51^r	Emission	Outflow
–	2.79	10.39	0.05	187 ± 7	429	64 ± 9	0.95 ± 0.23	11.67	19.35	Absorption	Inflow
–	2.76	10.48	0.08	185 ± 64	607	77 ± 44	0.74 ± 0.23	11.98	19.66	Absorption	Inflow
–	4.13	10.28	0.13	-191 ± 40	-199	187 ± 25	0.15 ± 0.23	12.96	20.64	Absorption	Outflow
–	4.50	10.32	0.03^b	-189 ± 21^b	-210^b	56 ± 48^b	0.56 ± 0.24^b	11.94^b	19.62^b	Absorption	Outflow
–	–	–	-0.11^r	191 ± 9^r	212^r	198 ± 6^r	-0.14 ± 0.25^r	12.89^r	20.56^r	Emission	Outflow
–	5.04	10.37	0.07^b	-185 ± 4^b	-227^b	50 ± 6^b	0.61 ± 0.22^b	12.30^b	19.98^b	Absorption	Outflow
–	–	–	-0.03^r	196 ± 43^r	241^r	197 ± 34^r	-0.32 ± 0.26^r	12.00^r	19.68^r	Emission	Outflow
–	5.32	10.46	0.04	204 ± 14	355	57 ± 19	0.32 ± 0.26	12.13	19.80	Absorption	Inflow
–	5.37	10.53	0.08	196 ± 13	444	69 ± 19	0.75 ± 0.24	11.99	19.67	Absorption	Inflow
–	5.23	10.61	0.11	174 ± 57	581	116 ± 28	0.68 ± 0.24	12.21	19.89	Absorption	Inflow
–	4.81	10.14	0.18	-237 ± 72	-247	299 ± 35	0.54 ± 0.24	12.51	20.19	Absorption	Outflow
–	8.18	10.41	0.19	-209 ± 64	-232	244 ± 18	0.28 ± 0.22	12.82	20.50	Absorption	Outflow
HIGH-*i*	2.68	10.41	0.02	189 ± 5	375	50 ± 2	0.94 ± 0.25	11.34	19.01	Absorption	Inflow
–	7.42	10.49	0.02	196 ± 25	368	51 ± 27	0.32 ± 0.27	11.88	19.56	Absorption	Inflow
–	1.69	10.71	0.04	187 ± 7	495	70 ± 10	0.87 ± 0.23	11.66	19.34	Absorption	Inflow
–	4.16	10.73	0.03	199 ± 6	424	56 ± 7	0.14 ± 0.24	12.44	20.12	Absorption	Inflow
–	11.02	10.79	0.05	210 ± 31	395	91 ± 34	0.40 ± 0.26	12.06	19.74	Absorption	Inflow
–	2.99	11.11	0.08	180 ± 19	443	81 ± 24	0.82 ± 0.25	11.96	19.63	Absorption	Inflow
–	8.55	11.07	0.03	189 ± 31	389	54 ± 33	0.73 ± 0.27	11.48	19.16	Absorption	Inflow
LOW-*i*	1.18	9.99	0.02^b	-234 ± 11^b	-293^b	53 ± 6^b	0.93 ± 0.24^b	11.13^b	18.81^b	Emission	Outflow
–	–	–	-0.22^r	20 ± 1^r	25^r	200 ± 0^r	-0.04 ± 0.00^r	14.34^r	22.02^r	Emission	Outflow
–	2.32	10.06	0.01^b	-266 ± 16^b	-328^b	59 ± 9^b	0.53 ± 0.16^b	11.22^b	18.90^b	Absorption	Outflow
–	–	–	-0.12^r	20 ± 2^r	25^r	199 ± 1^r	-0.02 ± 0.00^r	14.59^r	22.27^r	Emission	Outflow
–	1.52	10.33	0.01^b	-201 ± 7^b	-254^b	78 ± 10^b	0.33 ± 0.24^b	11.65^b	19.33^b	Absorption	Outflow
–	–	–	-0.27^r	20 ± 1^r	26^r	200 ± 1^r	-0.07 ± 0.01^r	13.76^r	21.43^r	Emission	Outflow
–	3.29	10.39	0.04	-193 ± 8^b	-241^b	–	–	–	–	P-Cygni	Outflow

Table B1 – *continued*

Sample	SFR	$\log M_*/M_\odot$	EW	Δv	$\Delta v/\cos(i)$	$b_{\rm D}$	$C_{\rm f}$	$N({\rm Na\,I})$	$N({\rm H})$	Profile	Type
–	–	–	-0.03	231 ± 13^r	288^r	–	–	–	–	P-Cygni	Outflow
–	8.67	10.48	0.06^b	-188 ± 45^b	-237^b	53 ± 28^b	0.71 ± 0.23^b	12.14^b	19.82^b	Absorption	Outflow
–	–	–	-0.04^r	195 ± 54^r	246^r	196 ± 44^r	-0.33 ± 0.27^r	12.04^r	19.72^r	Emission	Outflow
–	3.29	10.71	0.00^b	-226 ± 117^b	-284^b	57 ± 42^b	0.61 ± 0.28^b	10.39^b	18.07^b	Absorption	Outflow
–	–	–	-0.06^r	195 ± 5^r	245^r	200 ± 3^r	-0.68 ± 0.23^r	11.93^r	19.61^r	Emission	Outflow
–	7.54	10.74	0.04^b	-189 ± 2^b	-239^b	51 ± 5^b	0.93 ± 0.22^b	11.86^b	19.54^b	Absorption	Outflow
–	–	–	-0.07^r	189 ± 9^r	239^r	196 ± 5^r	-0.02 ± 0.29^r	13.58^r	21.25^r	Emission	Outflow
–	19.98	10.80	0.34	-157 ± 99	-200	188 ± 55	0.08 ± 0.28	13.95	21.63	Absorption	Outflow
–	12.93	11.07	0.20	-84 ± 103	-111	243 ± 43	0.77 ± 0.26	12.41	20.08	Absorption	Outflow
BULGE	1.21	10.02	-0.04	303 ± 26	393	84 ± 41	-0.53 ± 0.26	11.92	19.60	Emission	Outflow
–	2.73	10.08	0.10	-401 ± 88	-544	340 ± 58	0.25 ± 0.27	12.62	20.30	Absorption	Outflow
–	3.25	10.45	0.11	-163 ± 16	-219	196 ± 24	0.64 ± 0.24	12.25	19.93	Absorption	Outflow
–	8.20	10.47	0.25	-180 ± 32	-236	164 ± 24	0.10 ± 0.24	13.62	21.30	Absorption	Outflow
–	3.13	10.77	0.03	-177 ± 67	-248	75 ± 65	0.38 ± 0.27	11.99	19.66	Absorption	Outflow
–	8.20	10.79	0.29	-111 ± 23	-149	200 ± 17	0.17 ± 0.25	13.33	21.01	Absorption	Outflow
–	21.67	10.83	0.67	-145 ± 37	-202	266 ± 26	0.37 ± 0.22	13.36	21.04	Absorption	Outflow
–	31.86	11.11	0.47	-113 ± 117	-162	282 ± 61	0.14 ± 0.25	13.72	21.40	Absorption	Outflow
i-log SFR	4.85	10.48	0.15	-162 ± 19	-169	143 ± 30	0.71 ± 0.24	12.35	20.02	Absorption	Outflow
–	12.52	10.75	0.41	-158 ± 37	-164	214 ± 26	0.15 ± 0.24	13.63	21.30	Absorption	Outflow
–	2.44	10.21	0.06^b	-153 ± 6^b	-170^b	116 ± 13^b	0.48 ± 0.22^b	12.17^b	19.84^b	Absorption	Outflow
–	–	–	-0.05^r	195 ± 8^r	216^r	191 ± 5^r	-0.60 ± 0.24^r	11.92^r	19.60^r	Emission	Outflow
–	4.97	10.46	0.10^b	-192 ± 16^b	-213^b	149 ± 13^b	0.90 ± 0.21^b	12.06^b	19.73^b	Absorption	Outflow
–	–	–	-0.15^r	55 ± 23^r	61^r	117 ± 18^r	-0.62 ± 0.20^r	12.41^r	20.09^r	Emission	Outflow
–	12.80	10.70	0.36	-144 ± 35	-161	206 ± 19	0.16 ± 0.24	13.48	21.16	Absorption	Outflow
–	2.37	10.19	0.05	-157 ± 20	-194	55 ± 26	0.15 ± 0.26	12.86	20.54	Absorption	Outflow
–	4.94	10.46	0.12	-149 ± 9	-183	82 ± 17	0.06 ± 0.15	13.53	21.20	Absorption	Outflow
–	13.27	10.69	0.46	-69 ± 8	-84	152 ± 11	0.15 ± 0.02	13.74	21.42	Absorption	Outflow
–	13.15	10.77	0.23	-76 ± 16	-107	114 ± 16	0.05 ± 0.01	14.31	21.99	Absorption	Outflow
–	2.30	10.27	0.02	162 ± 28	283	50 ± 19	0.36 ± 0.26	12.21	19.88	Absorption	Inflow
–	2.19	10.30	0.06	150 ± 54	345	60 ± 37	0.23 ± 0.23	12.74	20.42	Absorption	Inflow
–	4.74	10.59	0.08	148 ± 4	338	53 ± 11	0.88 ± 0.24	12.36	20.04	Absorption	Inflow
–	12.42	10.82	0.10	145 ± 76	331	65 ± 47	0.26 ± 0.23	12.83	20.51	Absorption	Inflow
–	2.11	10.39	0.03	184 ± 59	606	57 ± 37	0.62 ± 0.25	11.70	19.38	Absorption	Inflow
–	4.52	10.68	0.10	146 ± 51	487	57 ± 31	0.36 ± 0.23	12.79	20.47	Absorption	Inflow
i-log M_*	3.62	10.30	0.15	-152 ± 26	-159	160 ± 35	0.58 ± 0.25	12.46	20.14	Absorption	Outflow
–	4.50	10.50	0.16	-146 ± 19	-152	173 ± 26	0.91 ± 0.24	12.27	19.94	Absorption	Outflow
–	6.42	10.69	0.24	-143 ± 24	-149	216 ± 38	0.60 ± 0.25	12.64	20.32	Absorption	Outflow
–	8.99	10.89	0.20	-178 ± 83	-184	250 ± 57	0.67 ± 0.26	12.50	20.18	Absorption	Outflow
–	2.52	10.11	0.01^b	-206 ± 85^b	-228^b	65 ± 42^b	0.74 ± 0.28^b	10.94^b	18.61^b	Absorption	Outflow
–	–	–	-0.09^r	198 ± 8^r	219^r	199 ± 7^r	-0.73 ± 0.26^r	12.12^r	19.80^r	Emission	Outflow
–	3.71	10.30	0.02^b	-173 ± 69^b	-192^b	71 ± 43^b	0.59 ± 0.25^b	11.75^b	19.43^b	Absorption	Outflow
–	–	–	-0.09^r	199 ± 11^r	222^r	199 ± 5^r	-0.20 ± 0.26^r	12.70^r	20.37^r	Emission	Outflow
–	4.95	10.49	0.13	-166 ± 12	-184	54 ± 36	0.10 ± 0.27	13.65	21.33	Absorption	Outflow
–	6.61	10.69	0.18	-146 ± 21	-162	187 ± 19	0.90 ± 0.24	12.34	20.02	Absorption	Outflow
–	8.09	10.88	0.17	-147 ± 23	-163	143 ± 28	0.42 ± 0.26	12.64	20.32	Absorption	Outflow
–	3.63	10.30	0.00^b	-234 ± 81^b	-287^b	86 ± 39^b	0.67 ± 0.26^b	10.80^b	18.48^b	Absorption	Outflow
–	–	–	-0.08^r	194 ± 32^r	238^r	195 ± 5^r	-0.02 ± 0.26^r	13.96^r	21.64^r	Emission	Outflow
–	4.89	10.50	0.03^b	-172 ± 62^b	-211^b	88 ± 35^b	0.34 ± 0.21^b	11.96^b	19.64^b	Absorption	Outflow
–	–	–	-0.08^r	150 ± 21^r	184^r	192 ± 11^r	-0.02 ± 0.02^r	14.47^r	22.15^r	Emission	Outflow
–	6.88	10.68	0.18	-130 ± 30	-159	117 ± 28	0.07 ± 0.29	13.63	21.31	Absorption	Outflow
–	8.03	10.88	0.06	-171 ± 42	-209	92 ± 26	0.73 ± 0.25	11.98	19.66	Absorption	Outflow
–	9.25	11.08	0.19	-108 ± 53	-132	182 ± 42	0.13 ± 0.27	13.28	20.96	Absorption	Outflow
–	8.03	10.88	0.04	-179 ± 106	-253	95 ± 65	0.33 ± 0.26	12.09	19.76	Absorption	Outflow
–	3.16	10.31	0.02	166 ± 20	288	50 ± 14	0.96 ± 0.27	11.60	19.27	Absorption	Inflow
–	7.46	10.88	0.04	148 ± 23	260	56 ± 34	0.64 ± 0.24	12.14	19.82	Absorption	Inflow
–	2.64	10.30	0.04	153 ± 33	346	51 ± 29	0.81 ± 0.25	12.17	19.84	Absorption	Inflow
–	3.66	10.50	0.04	162 ± 14	371	50 ± 8	0.84 ± 0.25	12.03	19.71	Absorption	Inflow
–	4.71	10.69	0.08	148 ± 20	342	50 ± 21	0.97 ± 0.24	12.43	20.11	Absorption	Inflow
–	6.17	10.87	0.09	148 ± 8	347	51 ± 22	0.49 ± 0.25	12.77	20.44	Absorption	Inflow
–	8.84	11.04	0.07	156 ± 113	365	73 ± 69	0.46 ± 0.26	12.34	20.01	Absorption	Inflow
–	3.15	10.51	0.05	160 ± 81	523	72 ± 52	0.56 ± 0.25	12.12	19.80	Absorption	Inflow
–	3.92	10.69	0.06	162 ± 28	543	60 ± 33	0.72 ± 0.24	12.16	19.84	Absorption	Inflow
–	5.33	10.86	0.11	153 ± 60	523	67 ± 40	0.95 ± 0.23	12.26	19.94	Absorption	Inflow

Table B2. The same as Table B1 but for AGN.

Sample	SFR	$\log M_*/M_\odot$	EW	Δv	$\Delta v/\cos(i)$	b_D	C_f	N(Na I)	N(H)	Profile	Type
DISK	0.34	10.81	-0.16	116 ± 87	120	185 ± 55	-0.82 ± 0.27	12.26	19.94	Emission	Outflow
–	0.26	10.87	0.02	174 ± 88	403	84 ± 67	0.68 ± 0.27	11.47	19.14	Absorption	Inflow
–	0.25	10.89	0.13	98 ± 25	356	181 ± 21	0.54 ± 0.24	12.37	20.05	Absorption	Inflow
–	0.25	10.94	0.22	132 ± 29	819	181 ± 28	0.52 ± 0.24	12.61	20.29	Absorption	Inflow
–	0.27	10.77	-0.03	180 ± 101	188	178 ± 59	-0.49 ± 0.26	11.79	19.47	Emission	Outflow
–	0.27	10.76	-0.02	191 ± 116	234	69 ± 71	-0.23 ± 0.26	11.86	19.54	Emission	Outflow
–	0.20	10.75	0.07	158 ± 22	376	165 ± 13	0.21 ± 0.26	12.52	20.20	Absorption	Inflow
–	0.23	10.79	0.11	165 ± 31	600	144 ± 15	0.94 ± 0.25	12.03	19.71	Absorption	Inflow
–	0.39	10.85	0.13	191 ± 31	1342	121 ± 22	0.67 ± 0.26	12.28	19.95	Absorption	Inflow
–	0.36	10.55	0.04	174 ± 30	415	96 ± 17	0.59 ± 0.25	11.82	19.49	Absorption	Inflow
–	0.39	10.61	0.08	169 ± 31	630	95 ± 24	0.63 ± 0.23	12.09	19.77	Absorption	Inflow
–	0.55	10.63	0.12	158 ± 30	1186	144 ± 21	0.62 ± 0.26	12.26	19.94	Absorption	Inflow
–	0.94	10.40	-0.04	250 ± 104	261	181 ± 50	-0.56 ± 0.26	11.87	19.55	Emission	Outflow
–	0.90	10.39	-0.05	158 ± 84	175	195 ± 38	-0.86 ± 0.25	11.72	19.40	Emission	Outflow
–	0.88	10.42	-0.03	296 ± 121	363	177 ± 62	-0.24 ± 0.25	12.10	19.78	Emission	Outflow
–	0.79	10.42	-0.02	290 ± 95	411	153 ± 65	-0.92 ± 0.25	11.37	19.05	Emission	Outflow
–	0.63	10.50	0.05	174 ± 43	413	96 ± 26	0.73 ± 0.24	11.77	19.45	Absorption	Inflow
–	0.71	10.59	0.07	179 ± 39	661	85 ± 27	0.69 ± 0.24	11.97	19.65	Absorption	Inflow
–	0.96	10.70	0.12	174 ± 24	1220	116 ± 16	0.34 ± 0.24	12.55	20.23	Absorption	Inflow
–	1.39	10.45	-0.06	185 ± 65	193	198 ± 40	-0.86 ± 0.26	11.85	19.53	Emission	Outflow
–	1.53	10.47	-0.06	170 ± 52	189	177 ± 36	-0.29 ± 0.24	12.30	19.98	Emission	Outflow
–	1.43	10.45	-0.06	210 ± 48	257	185 ± 29	-0.37 ± 0.26	12.19	19.87	Emission	Outflow
–	1.21	10.50	0.01	175 ± 144	306	66 ± 106	0.48 ± 0.28	11.27	18.94	Absorption	Inflow
–	1.10	10.55	0.05	186 ± 15	441	86 ± 18	0.20 ± 0.25	12.37	20.04	Absorption	Inflow
–	1.22	10.63	0.10	163 ± 15	599	112 ± 19	0.55 ± 0.19	12.23	19.90	Absorption	Inflow
–	1.44	10.72	0.12	177 ± 42	1255	95 ± 28	0.92 ± 0.26	12.09	19.76	Absorption	Inflow
–	2.14	10.40	-0.10	194 ± 25	216	207 ± 24	-0.35 ± 0.25	12.44	20.12	Emission	Outflow
–	2.11	10.50	0.01^b	-194 ± 108^b	-275^b	52 ± 43^b	0.67 ± 0.26^b	11.45^b	19.13^b	Absorption	Outflow
–	–	–	-0.05^r	193 ± 31^r	273^r	193 ± 26^r	-0.88 ± 0.23^r	11.70^r	19.38^r	Emission	Outflow
–	1.85	10.57	0.05	194 ± 47	462	63 ± 35	0.63 ± 0.25	11.84	19.52	Absorption	Inflow
–	1.90	10.60	0.08	179 ± 19	651	96 ± 21	0.31 ± 0.25	12.39	20.06	Absorption	Inflow
–	2.36	10.70	0.08	132 ± 94	875	111 ± 52	0.47 ± 0.25	12.22	19.90	Absorption	Inflow
–	4.23	10.45	0.16	-389 ± 67	-392	290 ± 80	0.88 ± 0.28	12.23	19.91	Absorption	Outflow
–	2.85	10.50	0.13	-238 ± 44	-249	248 ± 30	0.74 ± 0.27	12.22	19.89	Absorption	Outflow
–	3.12	10.43	0.07^b	-232 ± 26^b	-258^b	140 ± 19^b	0.43 ± 0.25^b	12.18^b	19.86^b	Absorption	Outflow
–	–	–	-0.07^r	190 ± 43^r	211^r	194 ± 36^r	-0.57 ± 0.27^r	12.06^r	19.74^r	Emission	Outflow
–	3.53	10.52	0.08^b	-209 ± 35^b	-257^b	156 ± 19^b	0.64 ± 0.24^b	12.08^b	19.75^b	Absorption	Outflow
–	–	–	-0.07^r	197 ± 48^r	243^r	197 ± 39^r	-0.23 ± 0.28^r	12.45^r	20.13^r	Emission	Outflow
–	3.41	10.53	0.08	-198 ± 39	-282	248 ± 12	0.72 ± 0.27	12.04	19.72	Absorption	Outflow
–	3.39	10.55	0.03	145 ± 85	256	126 ± 60	0.62 ± 0.25	11.73	19.41	Absorption	Inflow
–	3.14	10.57	0.07	151 ± 22	352	132 ± 20	0.79 ± 0.23	11.92	19.60	Absorption	Inflow
–	3.08	10.64	0.10	183 ± 17	642	86 ± 22	0.37 ± 0.23	12.44	20.12	Absorption	Inflow
–	4.80	10.44	0.37	-201 ± 30	-210	261 ± 33	0.64 ± 0.25	12.76	20.44	Absorption	Outflow
–	5.86	10.63	0.27	-242 ± 72	-271	300 ± 36	0.70 ± 0.26	12.58	20.26	Absorption	Outflow
–	6.15	10.59	0.27	-172 ± 76	-212	269 ± 37	0.18 ± 0.24	13.21	20.89	Absorption	Outflow
–	6.66	10.62	0.14	-406 ± 66	-582	442 ± 46	0.77 ± 0.27	12.23	19.91	Absorption	Outflow
–	6.35	10.66	0.08	197 ± 25	458	73 ± 26	0.75 ± 0.25	12.00	19.67	Absorption	Inflow
–	6.59	10.71	0.09	199 ± 23	712	71 ± 26	0.75 ± 0.25	12.08	19.75	Absorption	Inflow
–	11.69	10.57	0.53	-256 ± 96	-268	263 ± 55	0.21 ± 0.25	13.48	21.16	Absorption	Outflow
–	12.74	10.72	0.60	-258 ± 75	-286	304 ± 41	0.27 ± 0.25	13.42	21.09	Absorption	Outflow
–	13.38	10.67	0.35	-276 ± 88	-339	322 ± 57	0.22 ± 0.27	13.22	20.89	Absorption	Outflow
–	13.61	10.76	0.15	128 ± 62	289	146 ± 33	0.60 ± 0.22	12.38	20.06	Absorption	Inflow
–	11.43	10.69	0.11	142 ± 142	510	136 ± 96	0.95 ± 0.27	12.06	19.74	Absorption	Inflow
HIGH-*i*	2.82	10.47	0.03	199 ± 20	406	56 ± 21	0.52 ± 0.26	11.78	19.46	Absorption	Inflow
–	1.72	10.77	0.05	185 ± 9	449	90 ± 11	0.28 ± 0.24	12.28	19.95	Absorption	Inflow
–	4.64	10.78	0.04	188 ± 21	404	104 ± 21	0.94 ± 0.25	11.61	19.29	Absorption	Inflow
–	13.61	10.83	0.05	180 ± 116	368	112 ± 72	0.52 ± 0.26	11.94	19.62	Absorption	Inflow
–	2.61	11.10	0.09	145 ± 27	354	165 ± 20	0.80 ± 0.20	12.05	19.73	Absorption	Inflow
–	7.13	11.13	0.10	113 ± 59	249	161 ± 32	0.43 ± 0.23	12.36	20.04	Absorption	Inflow
–	23.11	11.11	0.13	159 ± 132	315	170 ± 82	0.83 ± 0.26	12.17	19.85	Absorption	Inflow
LOW-*i*	1.31	10.11	-0.05	308 ± 69	376	196 ± 49	-0.46 ± 0.26	12.03	19.71	Emission	Outflow
–	3.40	10.15	0.13	-355 ± 109	-442	383 ± 68	0.78 ± 0.25	12.22	19.89	Absorption	Outflow
–	0.53	10.39	-0.01	364 ± 127	462	55 ± 99	-0.71 ± 0.27	11.35	19.03	Emission	Outflow
–	1.53	10.41	0.03^b	-194 ± 80^b	-242^b	87 ± 39^b	0.55 ± 0.27^b	11.77^b	19.45^b	Absorption	Outflow
–	–	–	-0.19^r	21 ± 20^r	27^r	199 ± 5^r	-0.04 ± 0.00^r	13.98^r	21.66^r	Emission	Outflow

Table B2 *– continued*

Sample	SFR	$\log M_*/M_\odot$	EW	Δv	$\Delta v/\cos(i)$	b_D	C_f	$N(\mathrm{Na\,I})$	$N(\mathrm{H})$	Profile	Type
–	3.63	10.46	0.05^b	-222 ± 31^b	-279^b	184 ± 30^b	0.90 ± 0.25^b	11.69^b	19.37^b	Absorption	Outflow
–	–	–	-0.08^r	198 ± 9^r	249^r	199 ± 6^r	-0.16 ± 0.25^r	12.68^r	20.35^r	Emission	Outflow
–	10.11	10.52	0.20	-246 ± 70	-319	299 ± 30	0.93 ± 0.26	12.31	19.98	Absorption	Outflow
–	0.58	10.76	-0.02	173 ± 125	217	157 ± 76	-0.74 ± 0.27	11.29	18.97	Emission	Outflow
–	1.74	10.76	0.00^b	-250 ± 106^b	-313^b	66 ± 32^b	0.46 ± 0.16^b	10.75^b	18.43^b	Absorption	Outflow
–	–	–	-0.12^r	77 ± 8^r	97^r	200 ± 5^r	-0.03 ± 0.01^r	13.87^r	21.55^r	Emission	Outflow
–	4.60	10.77	0.05^b	-229 ± 29^b	-287^b	157 ± 18^b	0.46 ± 0.24^b	12.04^b	19.72^b	Absorption	Outflow
–	–	–	-0.08^r	199 ± 38^r	249^r	198 ± 33^r	-0.08 ± 0.27^r	13.02^r	20.70^r	Emission	Outflow
–	13.74	10.81	0.23	-336 ± 68	-438	348 ± 48	0.58 ± 0.27	12.58	20.26	Absorption	Outflow
–	42.22	10.81	0.66	-258 ± 63	-351	323 ± 47	0.42 ± 0.24	13.22	20.90	Absorption	Outflow
–	6.16	11.12	0.07	-426 ± 136	-550	443 ± 66	0.59 ± 0.26	12.04	19.72	Absorption	Outflow
–	18.91	11.12	0.44	-212 ± 111	-267	278 ± 52	0.09 ± 0.26	13.92	21.60	Absorption	Outflow
BULGE	0.83	10.07	-0.03	312 ± 73	395	142 ± 62	-0.86 ± 0.27	11.58	19.26	Emission	Outflow
–	2.27	10.07	0.15	-349 ± 81	-428	164 ± 86	0.03 ± 0.32	14.61	22.29	Absorption	Outflow
–	2.18	10.44	0.10	-195 ± 22	-253	228 ± 38	0.86 ± 0.25	12.08	19.76	Absorption	Outflow
–	6.01	10.49	0.27	-255 ± 24	-322	267 ± 27	0.71 ± 0.26	12.61	20.29	Absorption	Outflow
–	2.44	10.78	0.03	-488 ± 44	-700	449 ± 13	0.35 ± 0.25	11.89	19.57	Absorption	Outflow
–	6.76	10.80	0.19	-196 ± 42	-258	276 ± 24	0.86 ± 0.24	12.38	20.06	Absorption	Outflow
–	22.61	10.83	0.61	-227 ± 44	-300	233 ± 32	0.15 ± 0.25	13.91	21.58	Absorption	Outflow
–	12.44	11.08	0.21	-180 ± 107	-264	237 ± 55	0.05 ± 0.26	13.95	21.62	Absorption	Outflow
i-log SFR	5.78	10.65	0.24	-197 ± 35	-206	228 ± 40	0.68 ± 0.26	12.57	20.25	Absorption	Outflow
–	2.26	10.37	0.17	-160 ± 34	-178	208 ± 42	0.35 ± 0.26	12.74	20.42	Absorption	Outflow
–	5.32	10.63	0.26	-195 ± 25	-218	259 ± 25	0.92 ± 0.24	12.48	20.16	Absorption	Outflow
–	14.30	10.87	0.44	-235 ± 77	-262	305 ± 44	0.28 ± 0.26	13.28	20.96	Absorption	Outflow
–	2.33	10.32	0.21	-124 ± 28	-155	205 ± 24	0.27 ± 0.25	12.95	20.63	Absorption	Outflow
–	5.52	10.63	0.25	-133 ± 22	-163	210 ± 15	0.11 ± 0.24	13.50	21.18	Absorption	Outflow
–	15.17	10.90	0.32	-238 ± 82	-293	245 ± 45	0.11 ± 0.27	13.61	21.29	Absorption	Outflow
–	5.38	10.63	0.07	-370 ± 90	-529	387 ± 53	0.44 ± 0.27	12.24	19.92	Absorption	Outflow
–	15.16	10.83	0.12	-362 ± 95	-517	373 ± 71	0.89 ± 0.28	12.17	19.84	Absorption	Outflow
–	2.21	10.41	0.08	142 ± 34	250	69 ± 25	0.66 ± 0.22	12.27	19.95	Absorption	Inflow
–	2.08	10.45	0.11	139 ± 26	326	66 ± 16	0.33 ± 0.22	12.74	20.42	Absorption	Inflow
–	5.08	10.67	0.08	147 ± 10	343	50 ± 31	0.22 ± 0.26	13.09	20.77	Absorption	Inflow
–	2.13	10.48	0.05	193 ± 59	683	61 ± 33	0.31 ± 0.24	12.18	19.86	Absorption	Inflow
–	5.00	10.71	0.11	146 ± 56	509	53 ± 40	0.31 ± 0.24	13.01	20.69	Absorption	Inflow
–	12.34	10.95	0.12	183 ± 46	651	105 ± 28	0.45 ± 0.23	12.48	20.16	Absorption	Inflow
i-log M_*	1.58	10.12	0.08	-288 ± 117	-300	211 ± 96	0.53 ± 0.29	12.21	19.89	Absorption	Outflow
–	3.47	10.49	0.31	-193 ± 50	-200	256 ± 60	0.51 ± 0.28	12.83	20.51	Absorption	Outflow
–	7.76	10.67	0.42	-254 ± 36	-263	214 ± 38	0.12 ± 0.27	13.78	21.46	Absorption	Outflow
–	1.99	10.14	0.17	-149 ± 76	-165	190 ± 64	0.65 ± 0.27	12.44	20.12	Absorption	Outflow
–	2.92	10.36	0.15	-159 ± 26	-178	112 ± 35	0.67 ± 0.27	12.38	20.06	Absorption	Outflow
–	3.97	10.49	0.22	-281 ± 63	-311	309 ± 41	0.56 ± 0.27	12.63	20.31	Absorption	Outflow
–	5.80	10.70	0.29	-185 ± 32	-206	263 ± 36	0.97 ± 0.25	12.51	20.19	Absorption	Outflow
–	7.18	10.86	0.28	-165 ± 56	-183	238 ± 53	0.08 ± 0.27	13.79	21.47	Absorption	Outflow
–	10.45	11.05	0.37	-235 ± 51	-263	243 ± 58	0.30 ± 0.27	13.18	20.86	Absorption	Outflow
–	2.26	10.14	0.11	-159 ± 32	-197	118 ± 34	0.40 ± 0.27	12.48	20.15	Emission	Outflow
–	2.97	10.32	0.17	-141 ± 39	-172	182 ± 34	0.81 ± 0.25	12.35	20.02	Absorption	Outflow
–	4.30	10.50	0.18	-133 ± 49	-164	186 ± 30	0.10 ± 0.25	13.38	21.06	Absorption	Outflow
–	6.14	10.70	0.38	-113 ± 28	-138	200 ± 20	0.15 ± 0.25	13.59	21.27	Absorption	Outflow
–	7.24	10.90	0.26	-167 ± 44	-207	186 ± 26	0.08 ± 0.25	13.73	21.41	Absorption	Outflow
–	11.41	11.06	0.30	-160 ± 68	-198	220 ± 39	0.11 ± 0.26	13.61	21.29	Absorption	Outflow
–	4.01	10.50	0.14	-153 ± 81	-217	187 ± 54	0.04 ± 0.28	13.92	21.60	Absorption	Outflow
–	5.92	10.70	0.07	-221 ± 140	-318	186 ± 94	0.86 ± 0.27	11.95	19.63	Absorption	Outflow
–	8.74	10.87	0.23	-124 ± 118	-179	198 ± 68	0.05 ± 0.27	14.00	21.68	Absorption	Outflow
–	2.54	10.32	0.03	163 ± 117	288	52 ± 93	0.94 ± 0.28	11.84	19.51	Absorption	Inflow
–	8.06	11.09	0.06	146 ± 136	257	53 ± 90	0.55 ± 0.27	12.48	20.15	Absorption	Inflow
–	2.04	10.33	0.03	178 ± 108	422	61 ± 80	0.32 ± 0.26	12.06	19.74	Absorption	Inflow
–	3.51	10.51	0.03	174 ± 72	407	56 ± 39	0.48 ± 0.24	11.97	19.65	Absorption	Inflow
–	4.48	10.69	0.12	148 ± 37	343	51 ± 33	0.83 ± 0.23	12.65	20.33	Absorption	Inflow
–	6.44	10.89	0.07	146 ± 19	337	56 ± 31	0.62 ± 0.26	12.44	20.12	Absorption	Inflow
–	2.94	10.51	0.04	176 ± 74	645	100 ± 45	0.59 ± 0.24	11.89	19.56	Absorption	Inflow
–	4.33	10.69	0.06	167 ± 43	584	58 ± 34	0.81 ± 0.26	12.05	19.73	Absorption	Inflow
–	5.58	10.89	0.15	147 ± 61	501	58 ± 42	0.57 ± 0.23	12.76	20.44	Absorption	Inflow
–	6.98	11.09	0.18	146 ± 40	522	129 ± 24	0.62 ± 0.22	12.49	20.17	Absorption	Inflow

APPENDIX C: NA D PROFILES

In this section, we present examples of our Na D fits as described in Section 3.4 for the main sample of both inactive galaxies and the AGN sample.
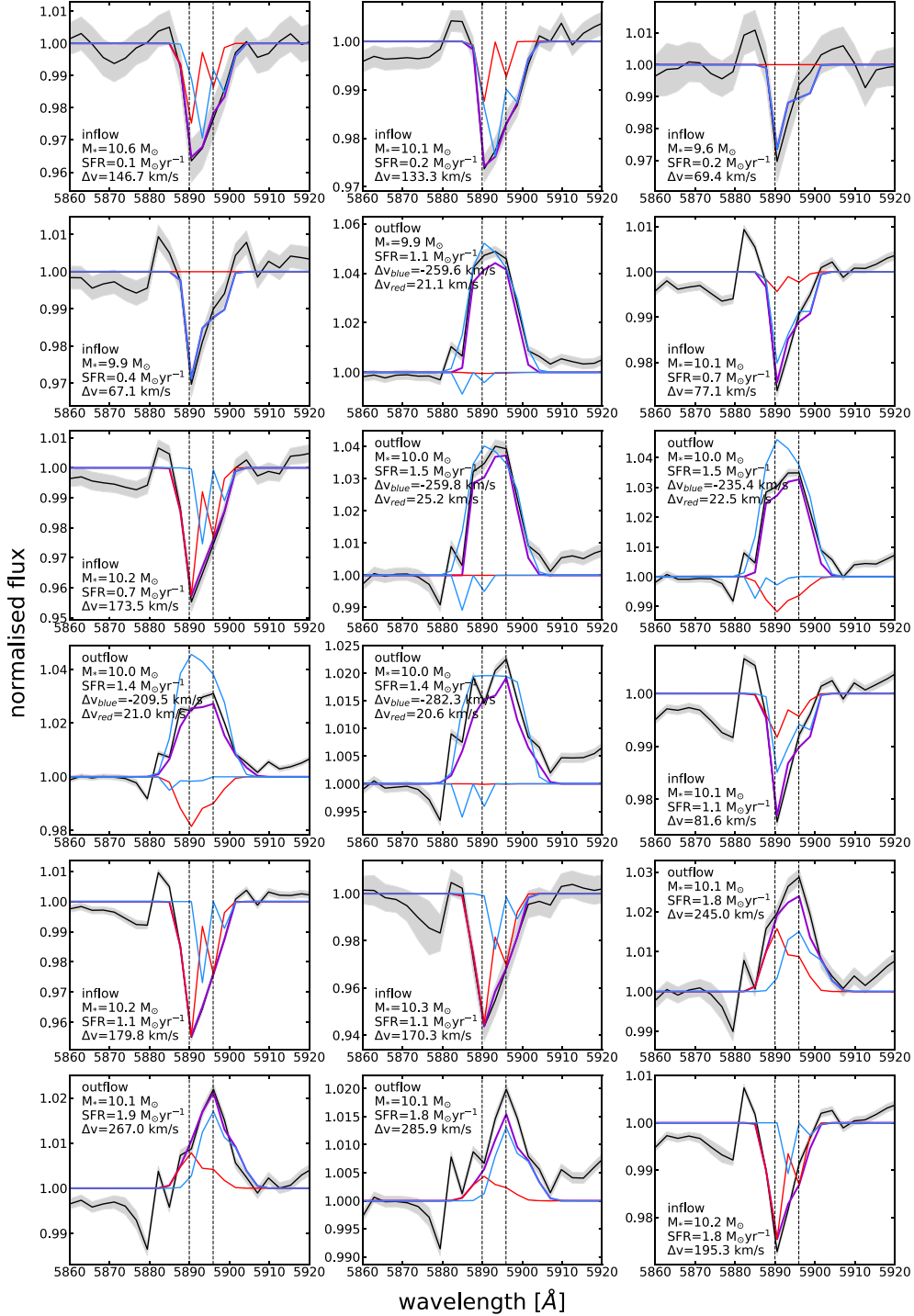

Figure C1.   The normalized Na D ISM profiles from inflow and outflow detections in the DISK, LOW-*i*, HIGH-*i*, and BULGE samples for inactive galaxies. The black line is the Na D profile and the grey shade is the flux error. The best-fitting two-component models are overplotted: purple denotes the total fit, red is the systemic component, and blue represents the blueshifted or redshifted flow component.
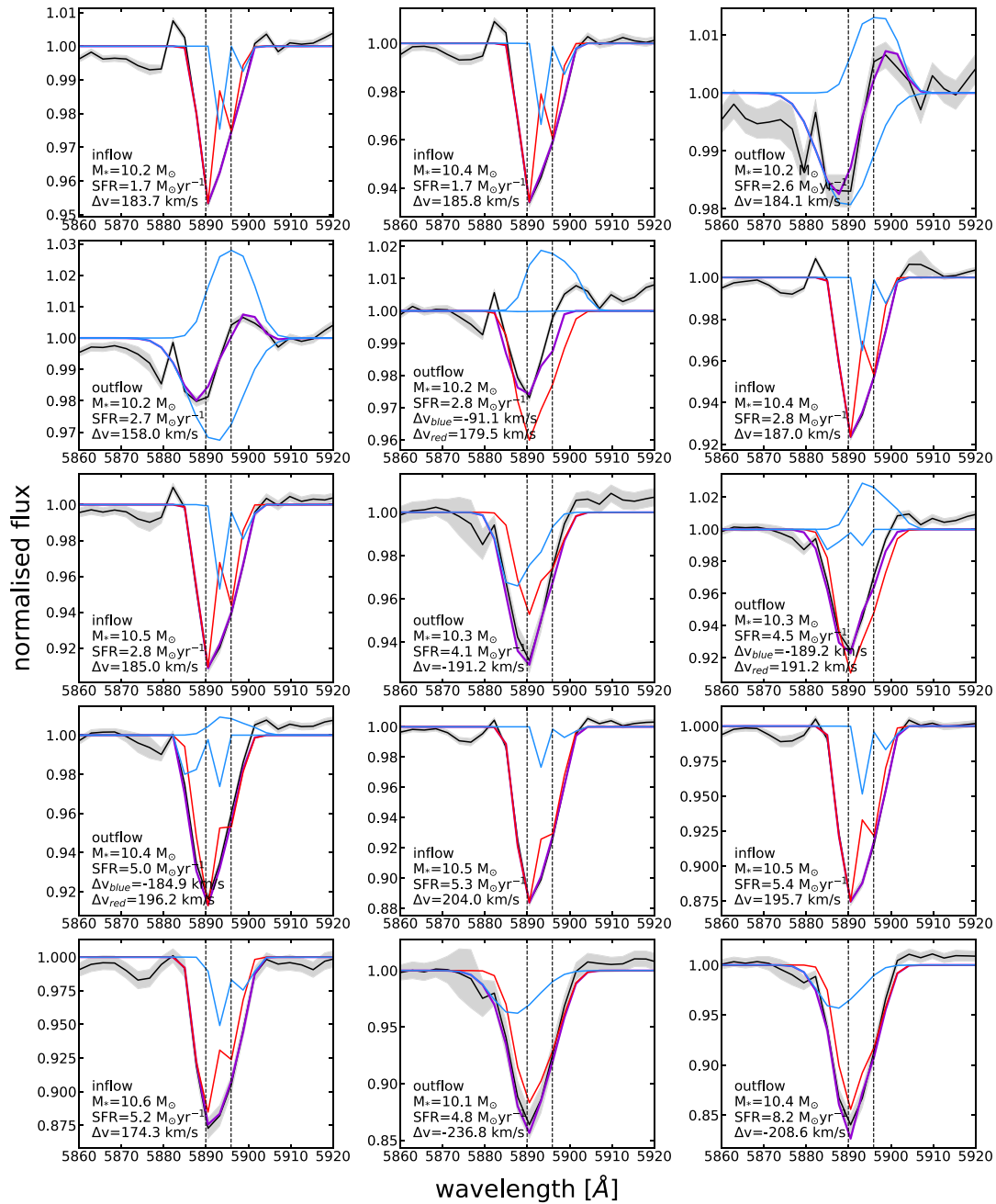
Figure C1 – *continued*
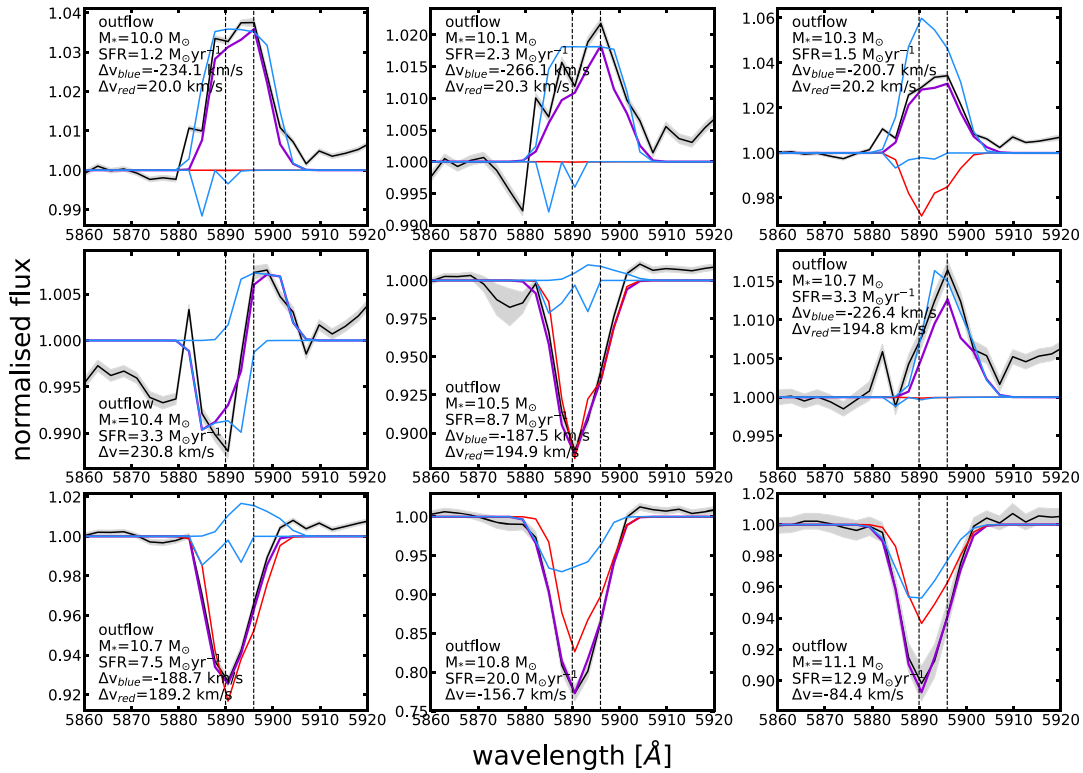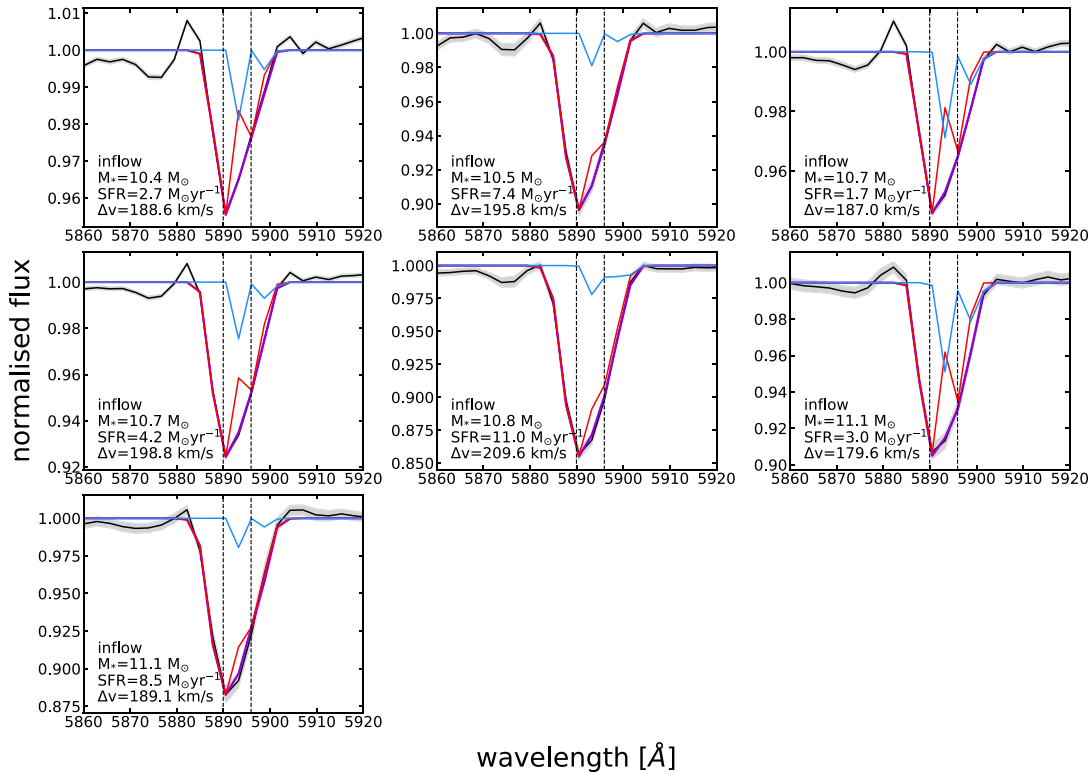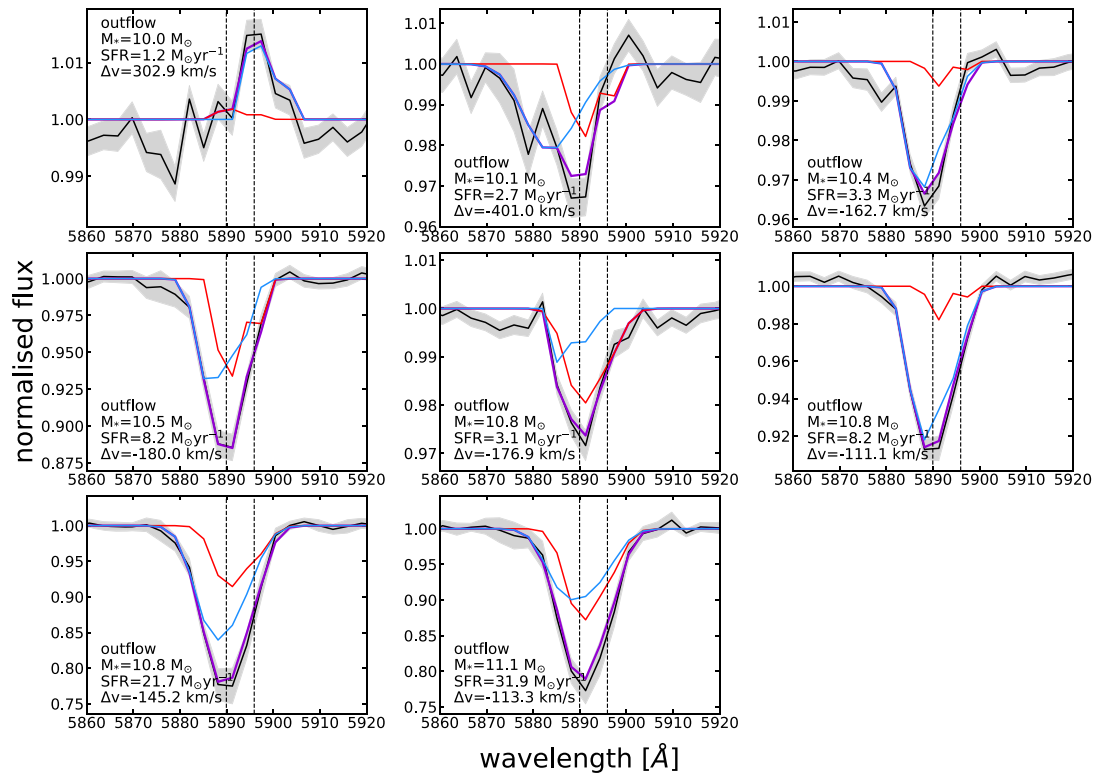
Figure C1 – *continued*

Figure C1 – *continued*

Figure C1 *– continued*

Figure C1 – *continued*

Figure C1 – *continued*

normalised flux

wavelength [Å]
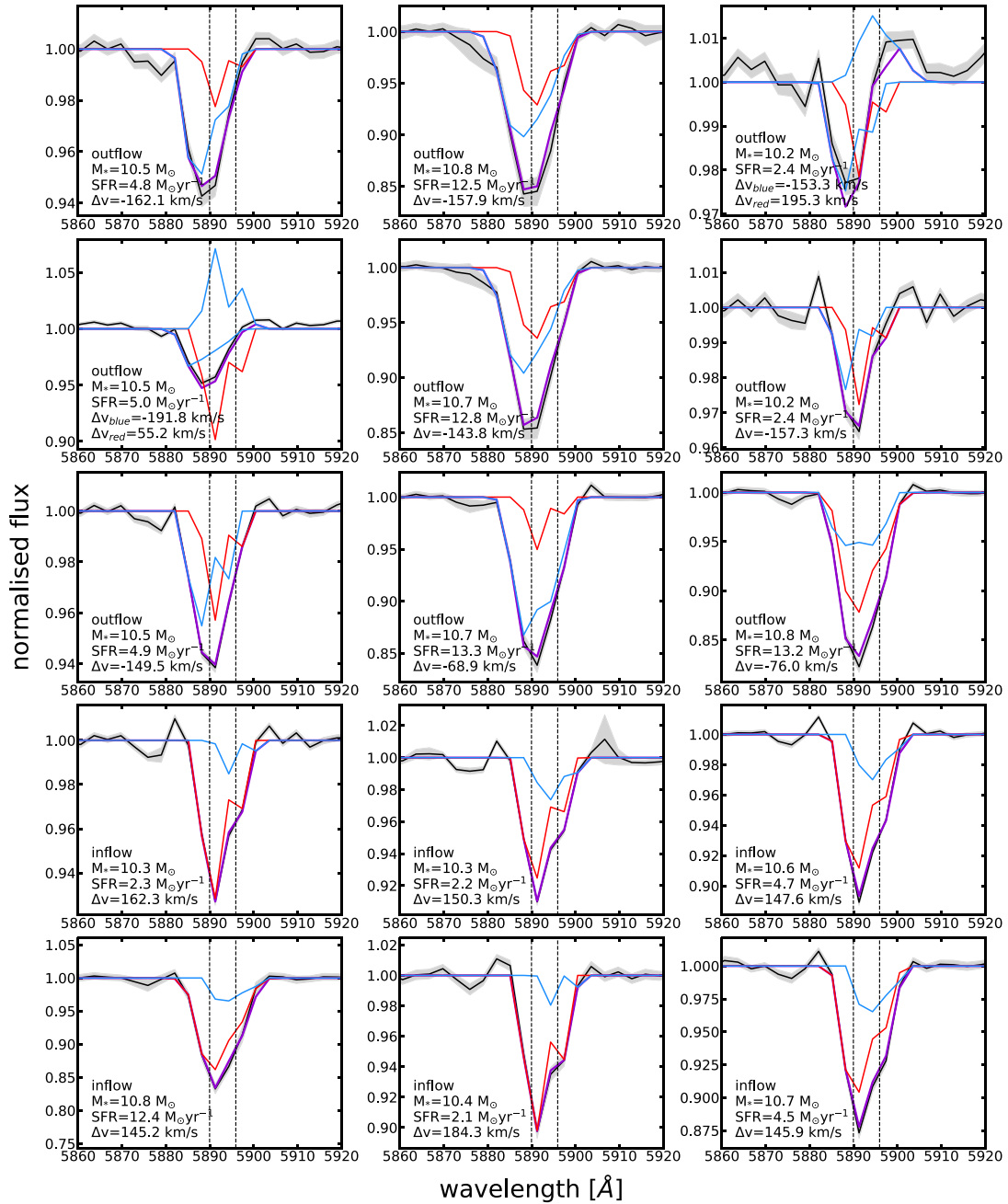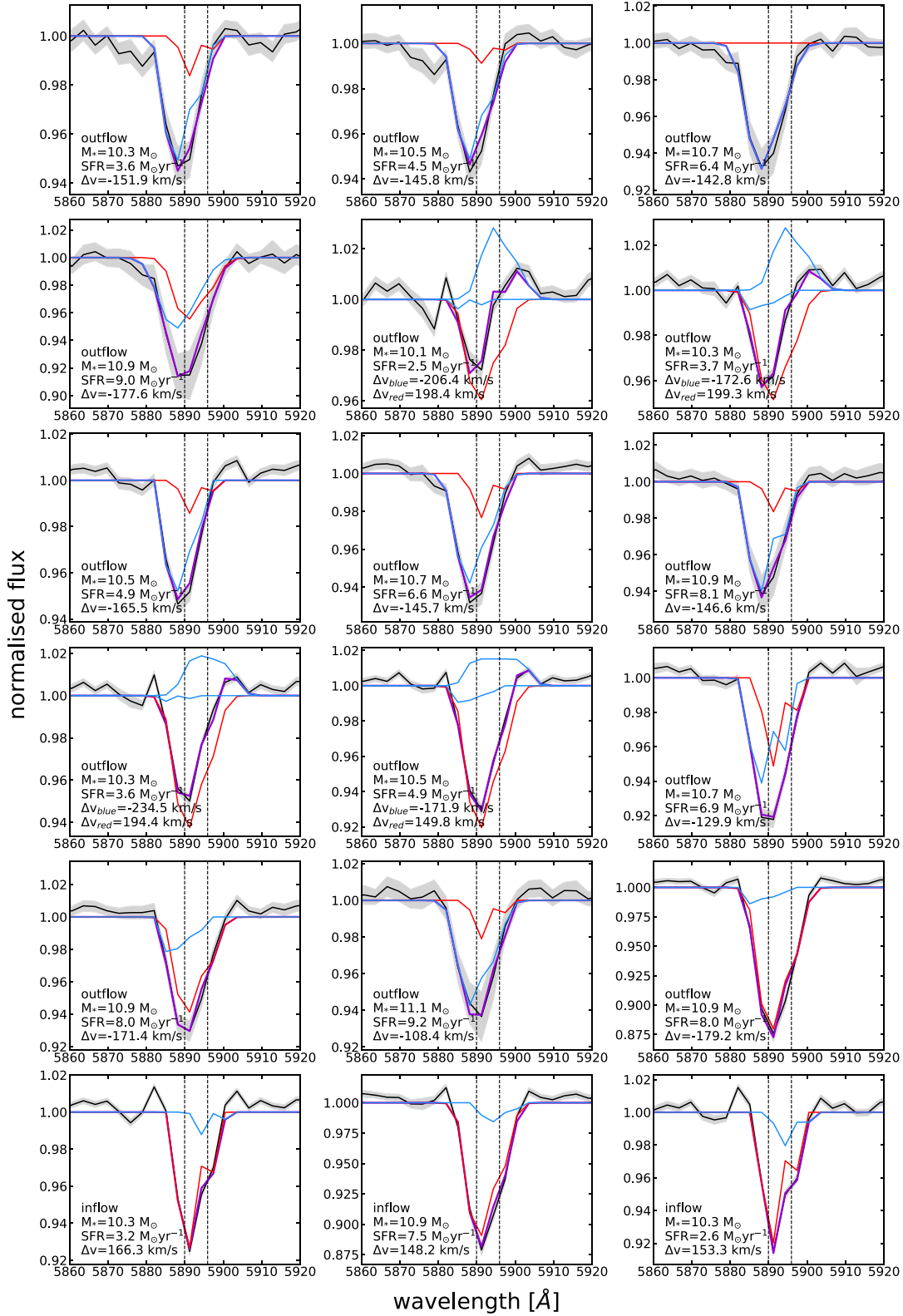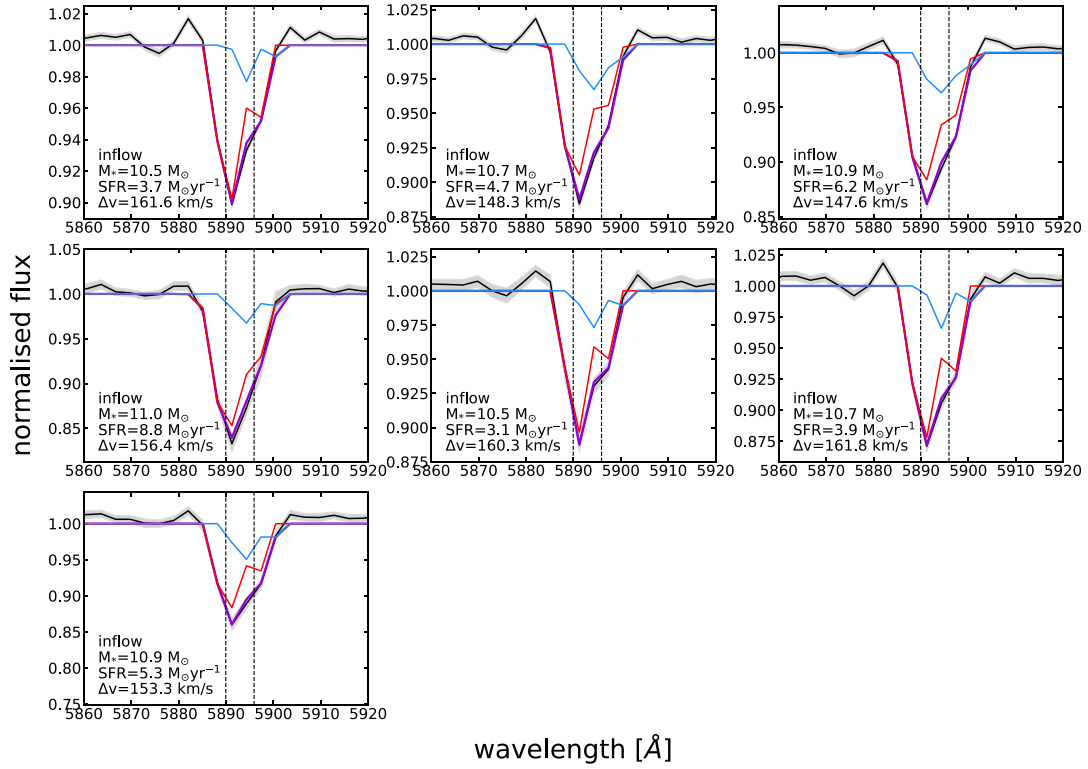
Figure C1 – *continued*
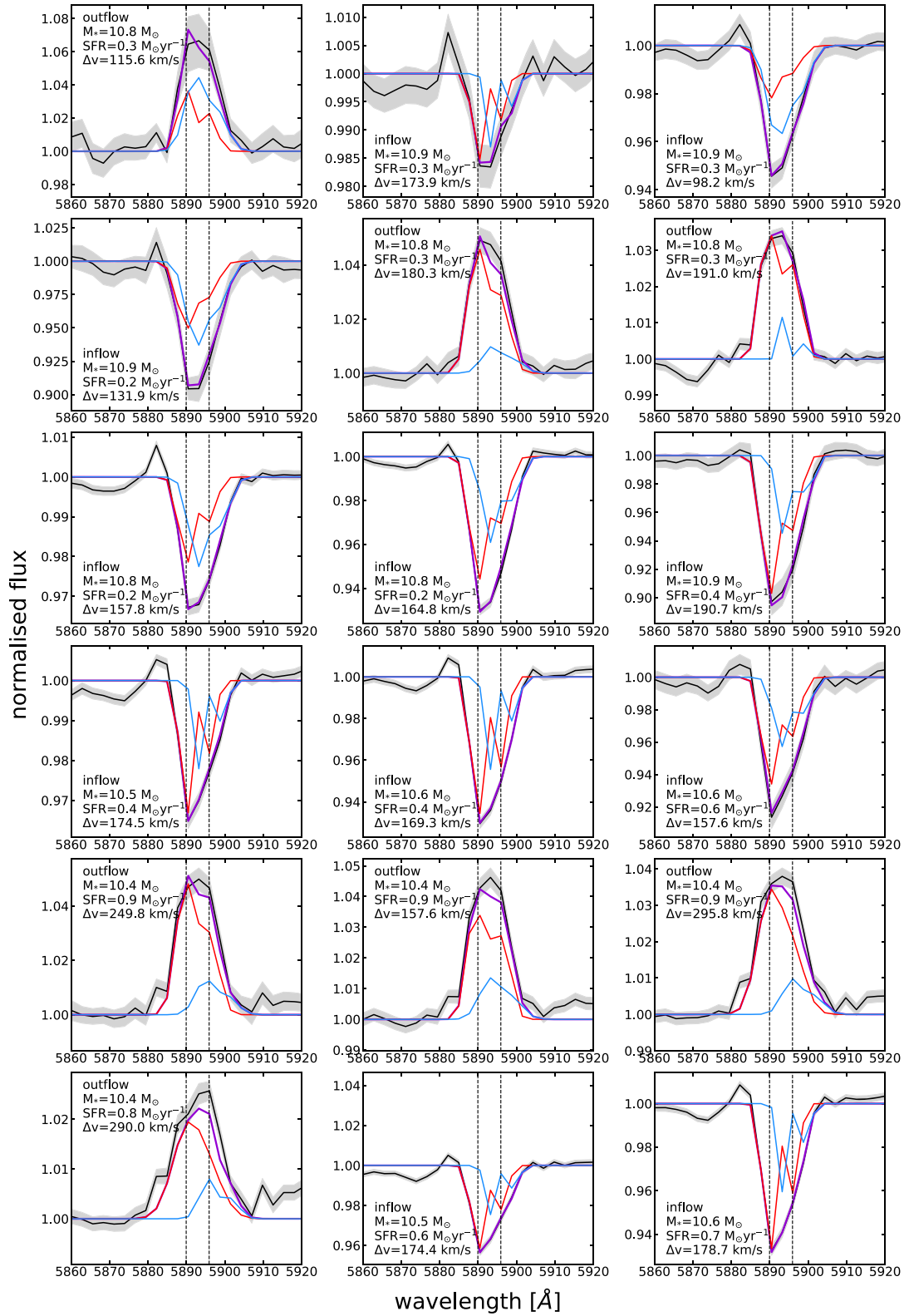
Figure C2. The same as Fig. C1 but for the AGN sample.
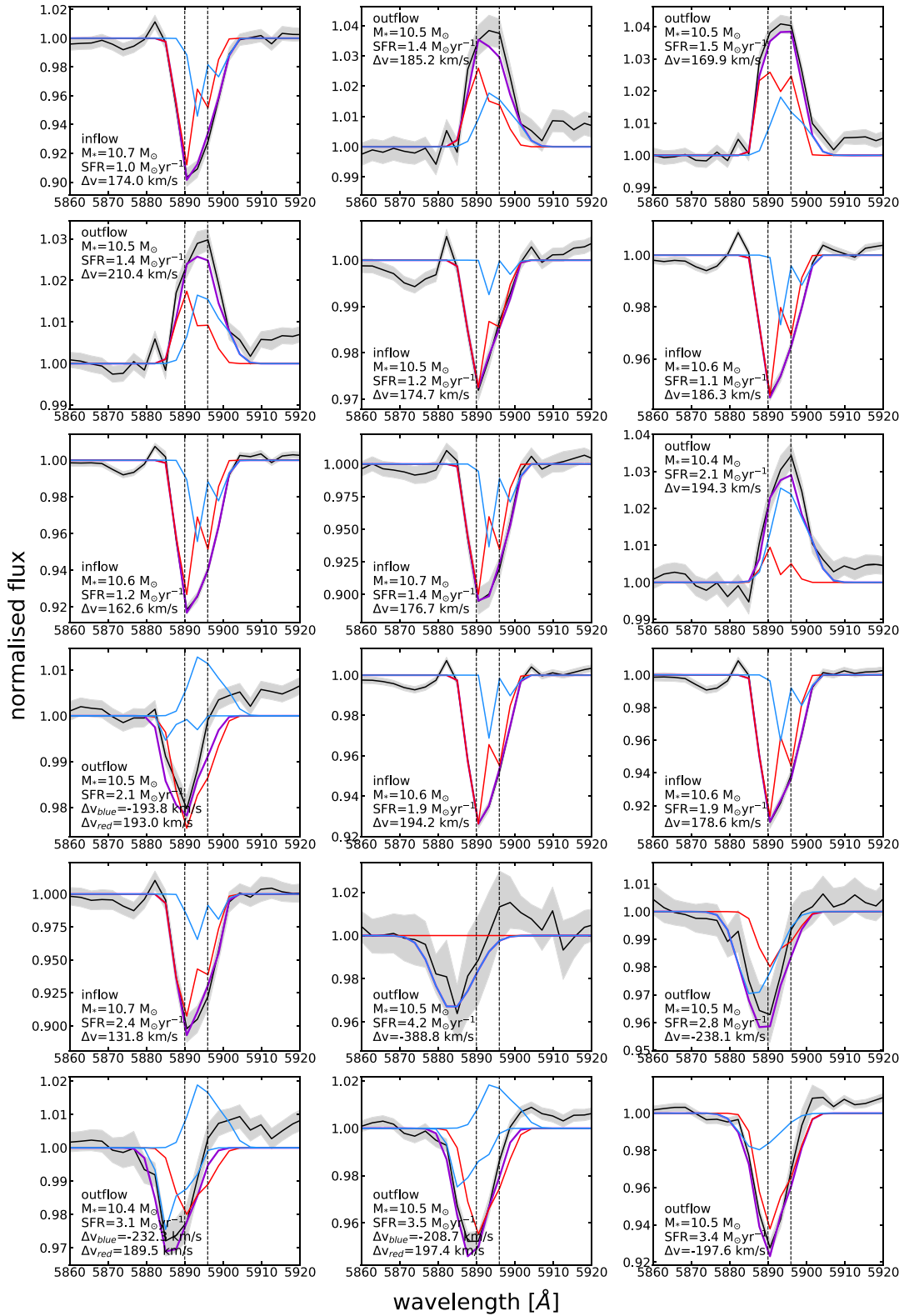
Figure C2 – *continued*
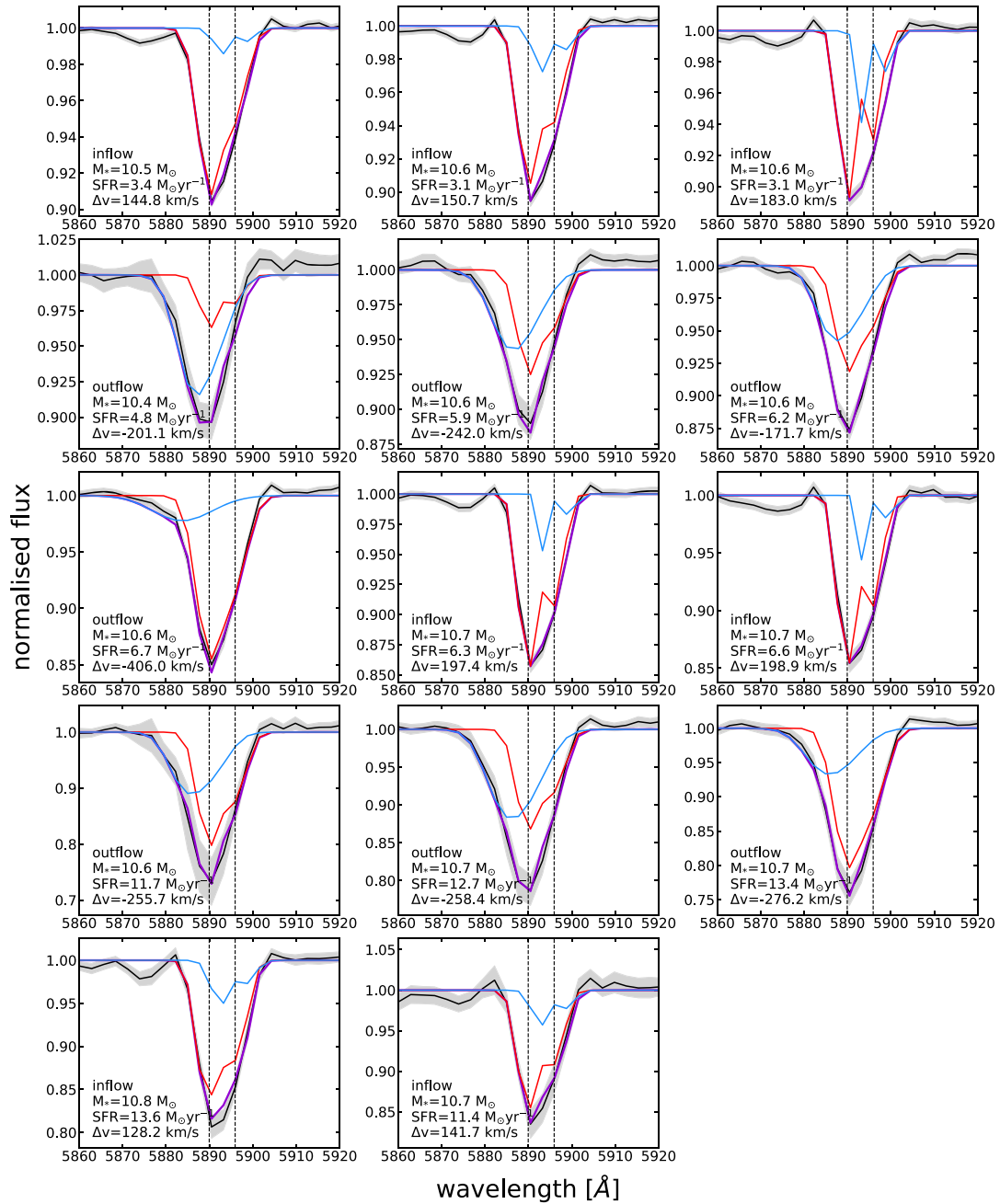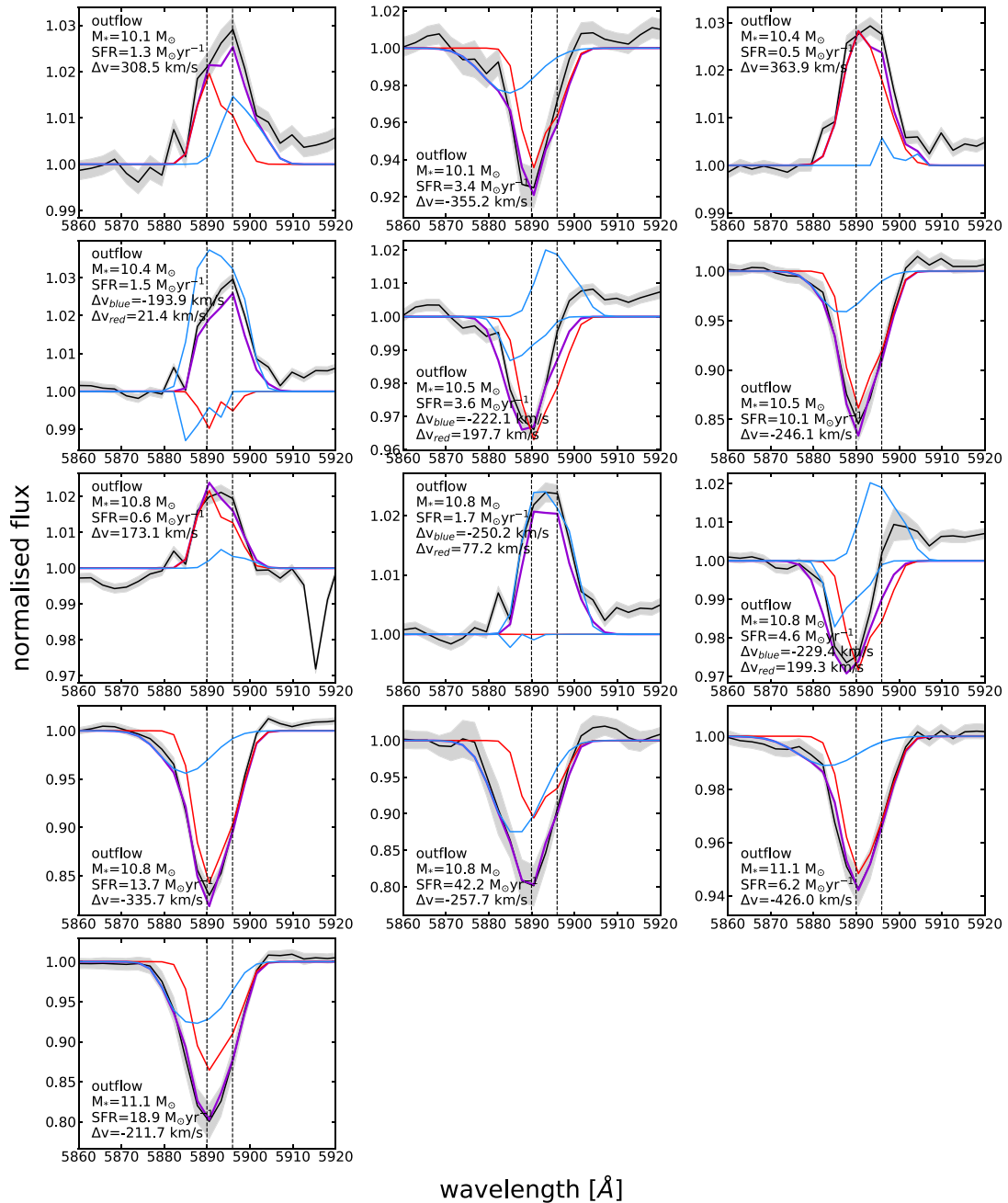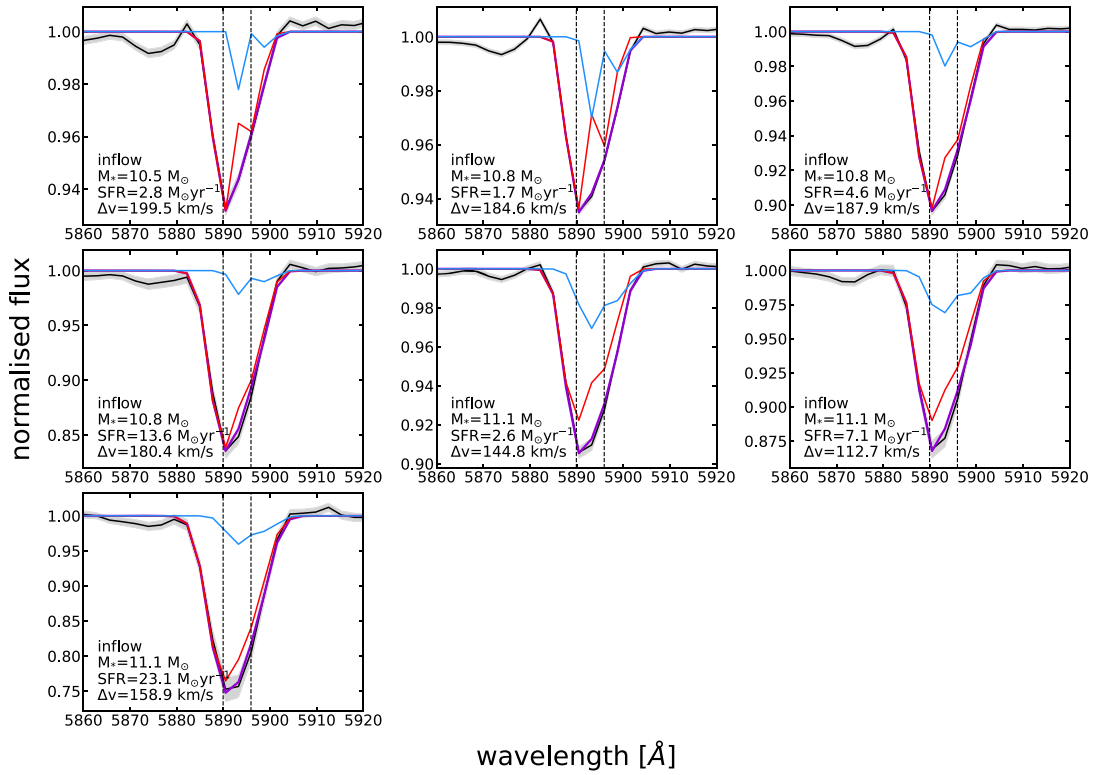
Figure C2 *– continued*

Figure C2 – *continued*

Figure C2 *– continued*
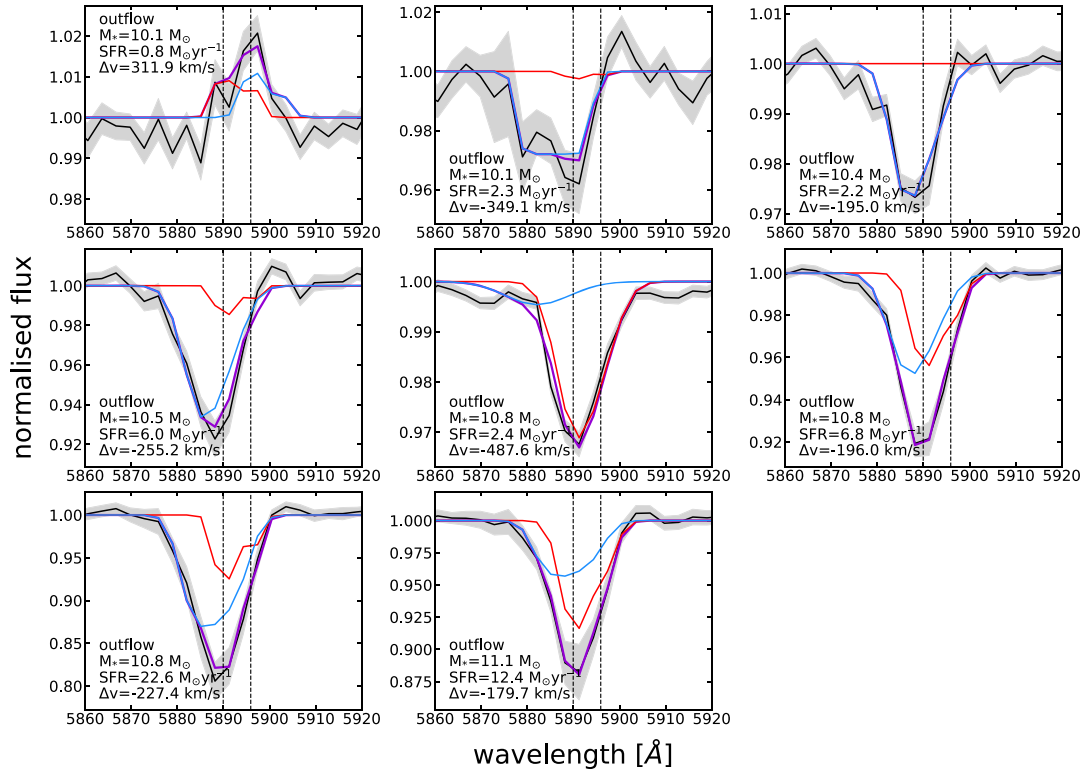
Figure C2 *– continued*
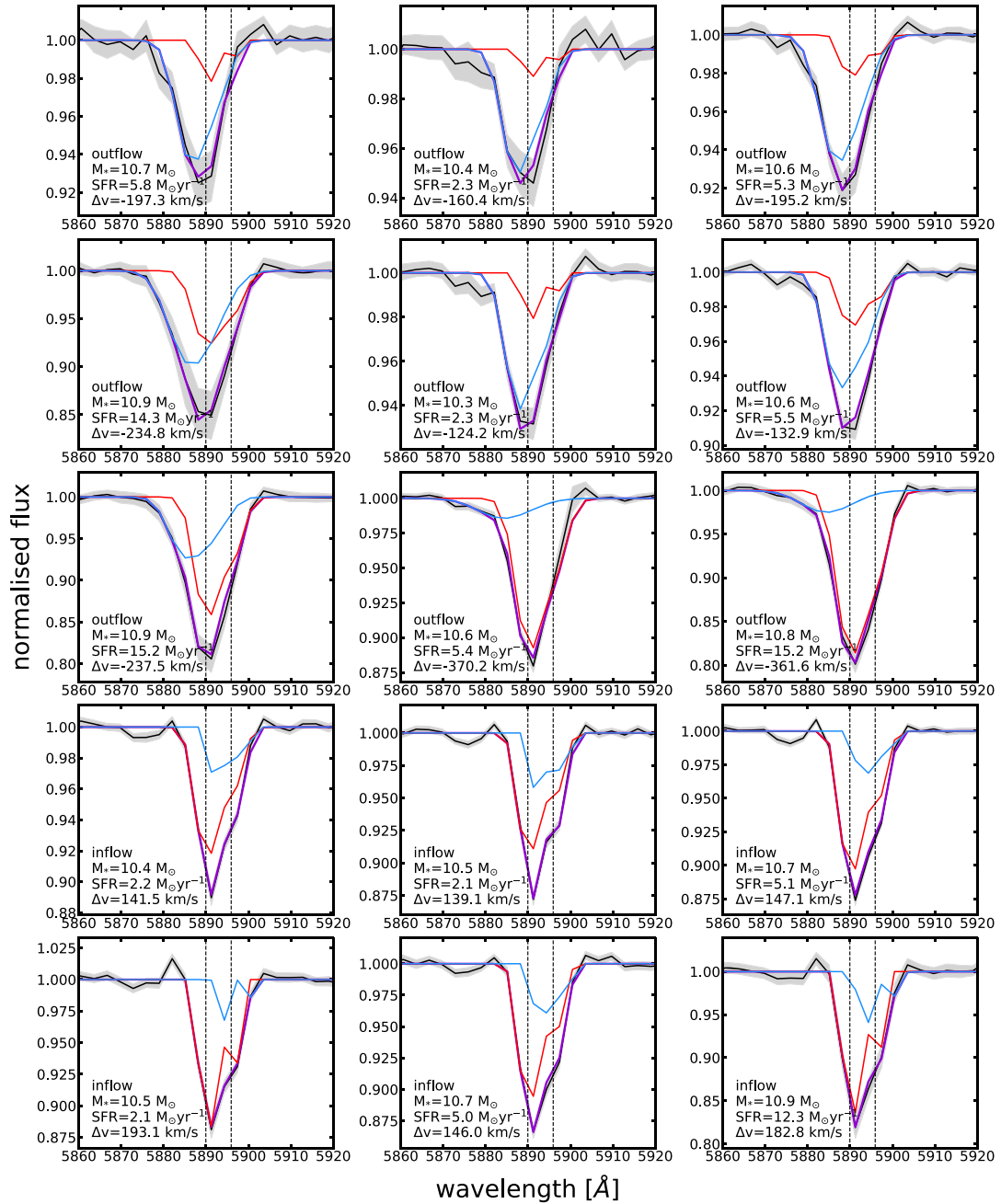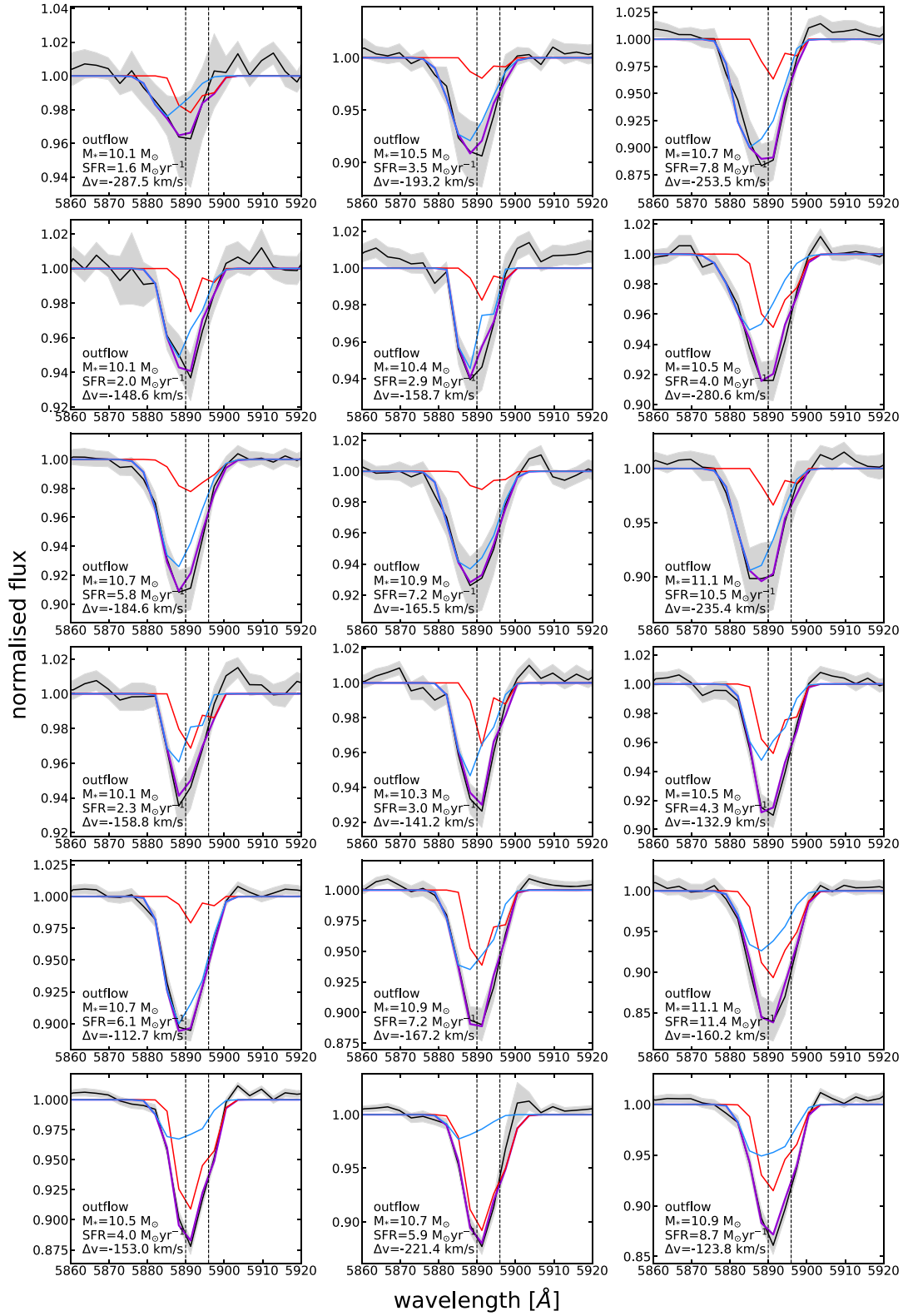
Figure C2 – *continued*
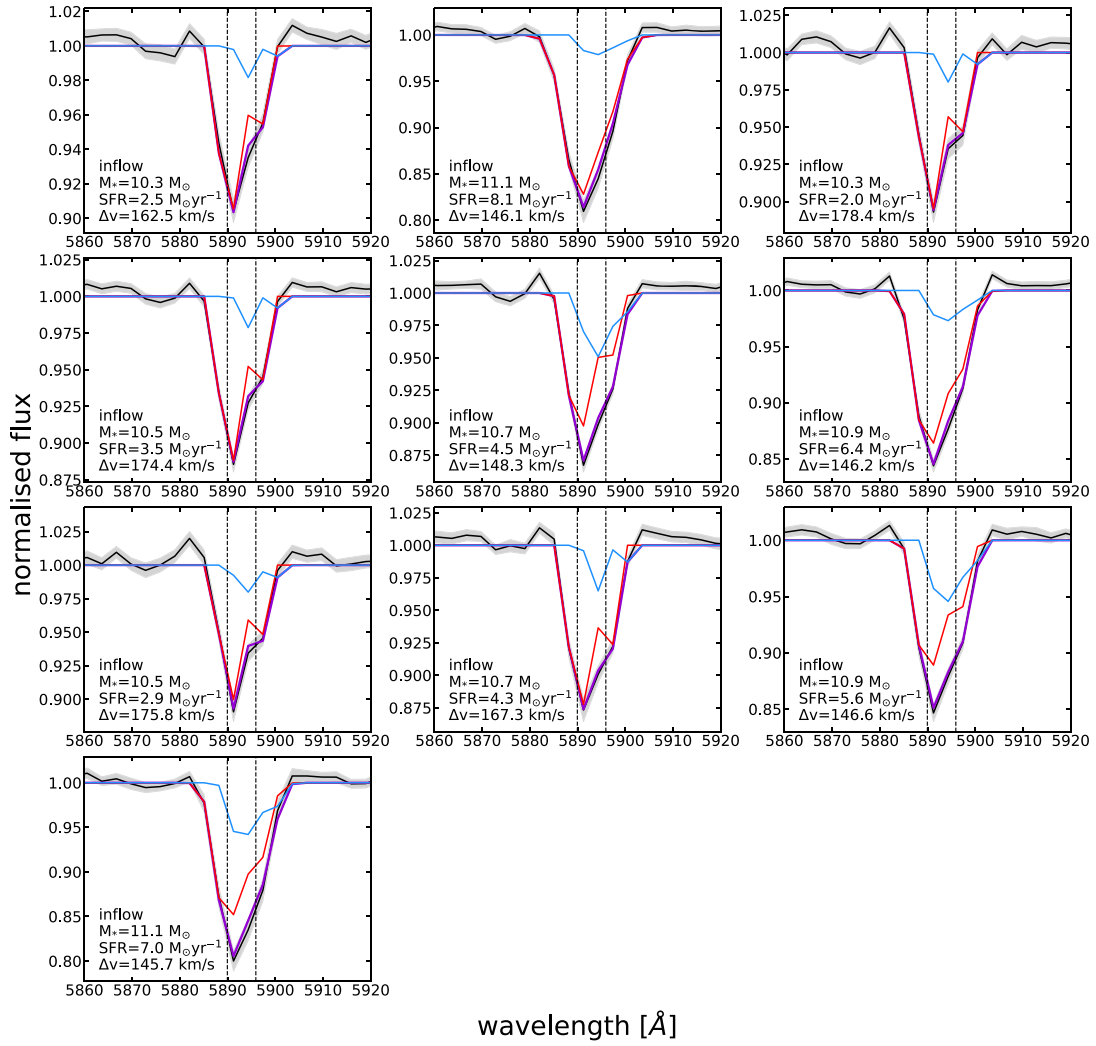
Figure C2 – *continued*

Figure C2 *– continued*

This paper has been typeset from a TEX/LATEX file prepared by the author.